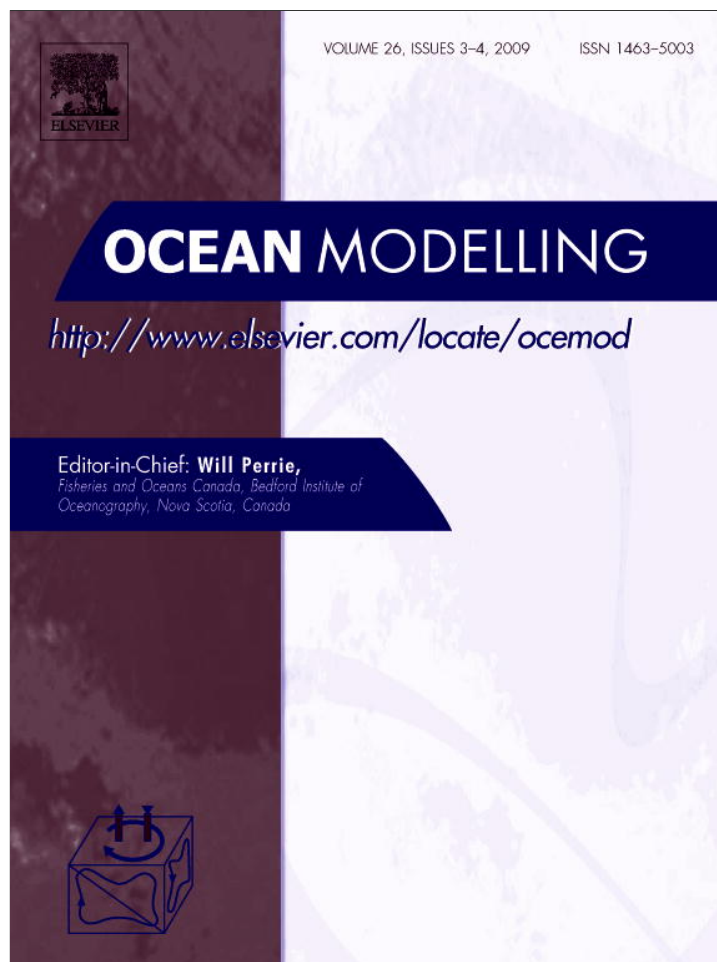


Provided for non-commercial research and education use.
Not for reproduction, distribution or commercial use.



This article appeared in a journal published by Elsevier. The attached copy is furnished to the author for internal non-commercial research and education use, including for instruction at the authors institution and sharing with colleagues.

Other uses, including reproduction and distribution, or selling or licensing copies, or posting to personal, institutional or third party websites are prohibited.

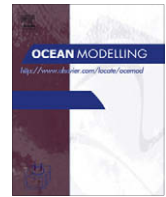
In most cases authors are permitted to post their version of the article (e.g. in Word or Tex form) to their personal website or institutional repository. Authors requiring further information regarding Elsevier's archiving and manuscript policies are encouraged to visit:

<http://www.elsevier.com/copyright>



Contents lists available at ScienceDirect

Ocean Modelling

journal homepage: www.elsevier.com/locate/ocemod

Large eddy simulation of stratified mixing in a three-dimensional lock-exchange system

Tamay M. Özgökmen^{a,*}, Traian Iliescu^b, Paul F. Fischer^c

^a RSMAS/MPO, University of Miami, Miami, FL, USA

^b Department of Mathematics, Virginia Polytechnic Institute and State University, Blacksburg, VA, USA

^c Mathematics and Computer Science Division, Argonne National Laboratory, Argonne, IL, USA

ARTICLE INFO

Article history:

Received 6 June 2008

Received in revised form 14 September 2008

Accepted 18 September 2008

Available online 10 October 2008

ABSTRACT

Accurate and computationally-efficient modeling of stratified mixing processes are of paramount importance in both coastal and large-scale ocean circulation. In this study, our main objective is to investigate the feasibility and accuracy of large eddy simulation (LES) as a possible tool to study small-scale oceanic processes. To this end, LES is evaluated in a 3D lock-exchange problem, which contains shear-driven mixing, internal waves, interactions with boundaries and convective motions, while having a simple domain, initial and boundary conditions, and forcing.

Two general classes of LES models are tested, namely eddy viscosity (EV) models based on constant-coefficient and dynamic Smagorinsky models, and an approximate deconvolution (AD) model. By noting that the dynamic Smagorinsky and AD models have different strengths in that the former is good in providing appropriate dissipation while the latter in preserving the detail of coherent structures on coarse resolution meshes, a hybrid approach combining EV and AD models is also evaluated. A direct numerical simulation (DNS) is performed as the benchmark solution, and all LES models are tested on three coarse meshes. The main measure of mixing is taken as the temporal evolution of background potential energy.

It is found that constant-coefficient Smagorinsky models can only provide a marginal improvement over under-resolved simulations, while both dynamic Smagorinsky and AD models lead to significant improvements in mixing accuracy. The primary accomplishment of this study is that it is shown that the hybrid approach attains the best agreement with the mixing curve from DNS, while being computationally approximately a thousand times faster.

© 2008 Elsevier Ltd. All rights reserved.

1. Introduction

Diapycnal mixing processes play a fundamental role in the dynamics of the ocean circulation. These processes are particularly important near the surface and the bottom of the ocean, near topographic features, near polar and marginal seas, as well as near the equatorial zones (Kantha and Clayson, 2000; Thorpe, 2005). In coastal waters, mixing is important for the transport and dispersion of biological species, and coastal discharges, while in the large scale flows, the irreversible changes in the water mass properties may have implications for the meridional overturning circulation (Munk, 1966; Munk and Wunsch, 1998).

There are at least three challenges in representing this fundamental process in coastal and ocean general circulation models (OGCMs). The first challenge is that the dynamics of stratified turbulent flows are complex and not very well understood. One can broadly classify them into a gravitationally-unstable regime or convection, stably-stratified shear flows, and internal waves. The

local gradient Richardson number, $Ri = N^2/S^2$, the ratio of the squares of buoyancy frequency and vertical shear, yields a commonly-used criterion, with $Ri < 0$ corresponding to convection, $0 \leq Ri < Ri_c$ to stably-stratified shear flows, and $Ri \geq Ri_c$ to the internal wave regime. The existence of a critical transition in mixing is commonly assumed by putting forth the concept of Ri_c , the value of which is typically $0.2 \leq Ri_c \leq 0.25$ based on theoretical (Miles, 1961) and some laboratory (Rohr et al., 1988) studies. Recent evidence from numerical simulations, oceanic and atmospheric observations reviewed by Canuto et al., (2008) indicates that mixing may persist for $Ri \gg Ri_c$, albeit at much reduced levels. As such, there is no definitive Ri_c beyond which stable stratification overpowers the vertical shear as to yield zero mixing. Fundamentally, it is not well understood how the transition between mixing and wave regimes takes place, or how these regimes interact with one another. The underlying issue is the strikingly different character of these two regimes: the turbulent mixing regime corresponds to one of local dissipation of momentum and energy, while the wave regime can transport momentum and energy over large distances, and possesses an inherently non-local character. While progress is being made (D'Asaro and Lien, 2000), the understanding of

* Corresponding author.

E-mail address: tozgokmen@rsmas.miami.edu (T.M. Özgökmen).

the interaction of wave and turbulence regimes still remains a significant problem.

The second challenge is the large range of scales in the ocean. Using a characteristic speed scale $U \approx 10^{-1} \text{ ms}^{-1}$, horizontal length scale $L \approx 10^5 \text{ m}$ and kinematic viscosity $\nu = 10^{-6} \text{ m}^2 \text{ s}^{-1}$, an upper limit for the Reynolds number $Re = UL/\nu$ can be obtained as $Re \approx 10^{10}$. Since the number of degrees of freedom in the case of homogenous, isotropic turbulence scales as $\sim Re^{9/4}$ (Lesieur, 1997), we obtain $\approx \mathcal{O}(10^{22})$ as an upper limit (namely without the limiting effects of stratification and rotation) for the needed number of spatial sampling points, at a given time. This has similar implications for both ocean modeling and observations in that it is challenging to digitally compute or physically sample accurately the state of the oceanic velocity and tracer fields in all spatial and temporal coordinates.

The third challenge arises from the interplay of the first two: it is not known with accuracy where and by which processes ocean mixing takes place. Ocean observations collected over the last decade highlighted the roles of topographic features in ocean mixing (Poltzin et al., 1997; Ferron et al., 1998; Ledwell et al., 2000; Nabatov and Ozmidov, 1988; Gibson et al., 1993; Lueck and Mudge, 1997; Kunze et al., 1997; Lavelle et al., 2004; Moum et al., 2002; Thurnherr and Speer, 2003; Thurnherr et al., 2004; Thurnherr, 2006). As such, knowledge of bathymetry with high accuracy is also needed in order to achieve an accurate representation of diapycnal mixing. The large range of scales applies to bathymetry as well, in that sea-floor morphology shows variability at almost all spatial scales (Weissel et al., 1994).

Given the large range of scales in the ocean, one promising approach to overcome these challenges is *multi-scale* modeling. For instance, for large-scale simulations, second-order closure (SOC) models are most appropriate for OGCMs. SOC models (Wilcox, 1998) are based on time averaging of the Navier–Stokes equations and the decomposition of the state variables into mean and fluctuating (or turbulent) components (so-called Reynolds decomposition). In addition to the primary flow field equations, differential equations for turbulent kinetic energy, and some combination of turbulent length scale, dissipation rate, or turbulent frequency are integrated in time to calculate eddy-viscosity and eddy diffusivity in these models. There has been a steady improvement in turbulence closure models for oceanographic applications (Mellor and Yamada, 1982; Kantha and Clayson, 1994; Burchard and Baumert, 1995; Burchard and Bolding, 2001; Canuto et al., 2001; Baumert and Peters, 2004; Baumert et al., 2005; Warner et al., 2005; Umlauf and Burchard, 2005; Canuto et al., 2007). While algebraic closures such as K-Profile Parameterization (KPP, Large et al. (1994), Large and Gent (1999)), in which the vertical viscosity/diffusivity is a specified function of Ri , are also widely used in OGCMs at the present time, the performance of the SOC models is shown to be superior to that of algebraic closures in some demanding cases, such as overflows (Ilicak et al., 2008a).

The hydrostatic approximation commonly used in OGCMs is adequate for large-scale ocean dynamics, but it is expected to break down for scales smaller than a few km (Kantha and Clayson, 2000), such as in most coastal-scale applications and in high-resolution modeling of isolated mixing processes. High-resolution hydrostatic models start to exhibit unphysical behavior in a flow regime where vertical accelerations are comparable to hydrostatic pressure gradients (Fringer et al., 2006). Also, the dispersion relations for internal waves differ in hydrostatic and non-hydrostatic cases. Thus, hydrostatic models not only have errors in representing the shape of the internal waves (Horn et al., 2001), but they can also fail to represent the wave-induced boundary mixing (Boegman et al., 2003; Bourgault and Kelly, 2003). As such, it is not clear yet how the interaction of internal wave motions and mixing can be accurately represented in hydrostatic models.

A relatively new approach in ocean modeling is *large eddy simulation* (LES), which relies on the spatial filtering of the (non-hydrostatic) Navier–Stokes equations. The fundamental idea in LES is to compute the large eddies, which carry out most of the mixing and transport, are inhomogeneous, long-lived, depend on model geometry and are thus difficult to model analytically. On the other hand, the smaller eddies are more isotropic, homogeneous, short-lived, universal and thus more amenable to theoretical modeling (Schumann, 1991). Since the resolution of the smallest scales is avoided, the computational cost of LES can be several orders of magnitude less than that of direct numerical simulation (DNS), in which all dynamical scales of motion are computed.

In particular, we envision two main possible roles for LES in ocean modeling:

- (i) Output from LES can serve as benchmark solutions for SOC models (e.g., Canuto et al., 2008). This is especially suitable for helping test the accuracy of SOC in mixing processes that are important for the large-scale circulation, for which LES is not expected to be feasible in the foreseeable future.
- (ii) In light of the continuous growth of computer power and the non-hydrostatic resolution limit encountered by hydrostatic models, LES may become a feasible avenue for coastal modeling.

Before undertaking these major tasks, however, one first needs to carefully evaluate the accuracy and computational efficiency of the LES methodology in problems involving stratified mixing.

Therefore, our main objective in this study is to investigate and quantify the success of LES in the case of stratified mixing. Instead of taking the more conventional route of applying LES in an oceanographic setting and comparing with observational results, we set up a canonical benchmark problem, the *lock-exchange problem* in an enclosed box domain. In this problem, the vertical barrier separating two fluids of different densities is abruptly removed, and counter-propagating gravity currents initiate mixing via shear. The time evolution of the lock-exchange problem in an enclosed domain is quite complex, showing shear-driven mixing, internal waves interacting with the flow field and the solid boundaries, gravitationally-unstable phases and flow transients. Yet, the problem involves simple and unambiguous forcing, initial and boundary conditions. The rationale for our choice is that, in oceanic cases, the scarcity of observations and the uncertainties due to sampling errors of measurements, forcing, initialization, and boundary conditions can obscure the effect of LES modeling. The lock-exchange setup has long served as a paradigm configuration for studying the spatiotemporal evolution of gravity currents. This benchmark problem has been investigated both experimentally (Britter and Simpson, 1978; Simpson, 1979; Huppert and Simpson, 1980; Rottman and Simpson, 1983; Hallworth et al., 1993, 1996; Hacker et al., 1996) and theoretically (Benjamin, 1968; Shin et al., 2004). The direct numerical simulations of Härtel et al. (2000), Cantero et al. (2006), and Cantero et al. (2007) provided detailed information on the dynamics of the lock-exchange problem.

Two different classes of LES models are tested in the numerical approximation of mixing in the lock-exchange problem: a set of eddy-viscosity models (Smagorinsky, 1963), and an approximate deconvolution model (Galdi and Layton, 2000). The novel feature of the approximate deconvolution model is that its derivation is strictly mathematical, and is not based on phenomenological assumptions. The eddy-viscosity models tested consist of the classical Smagorinsky model, a version in which the stresses in the active scalar equation depend on the Ri (Özgökmen et al., 2007), and the dynamic Smagorinsky model (Germano et al., 1991), which is adapted to the high-order polynomial discretization scheme of the hydrodynamic model used here. We also experiment with

mixed and hybrid models. We perform a thorough *a posteriori* testing of the LES models by using the background potential energy as the main measure for the cumulative result of stratified mixing processes. To this end, we first perform a DNS as the benchmark solution. LES is run on three coarse meshes, for which also under-resolved DNS (denoted DNS* here) are conducted, in which no SGS model is used.

We show that constant-coefficient Smagorinsky models lead only to marginal improvements, whereas the dynamic Smagorinsky model and the approximate deconvolution model result in significant increases of accuracy in the prediction of mixing. It is found that the hybrid model, in which the dynamic Smagorinsky and approximate deconvolution models are used together to form the SGS momentum stress tensor, reproduces the mixing curve from DNS, while attaining approximately 1212-fold gain in computation time.

All numerical experiments in this study are carried out with Nek5000, the high-order spectral element model developed by Fischer (1997), Fischer et al. (2000). This model combines the geometrical flexibility of finite element models with the numerical accuracy of spectral models in a way that is especially suitable for parallel computing environments. While the box-shaped domain does not employ the geometrical flexibility of this model, high-order numerical accuracy is critical to avoid numerical dissipation and dispersion errors in order to isolate the net effect of the SGS models. Scalability is necessary for DNS and convenient for LES calculations.

The paper is organized as follows: the concept of LES and the SGS models tested in this study are discussed in Section 2. A short description of the numerical model Nek5000 is given in Section 3. The model configuration and the parameters of the numerical experiments are outlined in Section 4. Results are presented in Section 5. Finally, the principal findings and future directions are summarized in Section 6.

2. Large eddy simulation of stratified flows

The underlying idea of LES is based on the observation that most of the mixing in turbulent flows is carried out by coherent structures (namely, large eddies). Since the characteristics of these coherent structures change significantly from one flow type to another, these eddies must be modeled through computation. Imbedded in these large eddies are smaller eddies, which arise from the instabilities of the large eddies. These small eddies tend to have a much more universal character and thus, they are more conducive for parameterizations. Below we present a short review of LES. The reader is referred to Sagaut (2006) and Berselli et al. (2005) for an extensive review of the recent LES literature.

We use the Boussinesq equations:

$$\begin{cases} \frac{D\mathbf{u}}{Dt} + \frac{1}{\rho_0} \nabla p - \nu \Delta \mathbf{u} + \frac{\rho'}{\rho_0} \mathbf{g} = \mathbf{k} = 0, \\ \nabla \cdot \mathbf{u} = 0, \\ \frac{D\rho'}{Dt} - \kappa \Delta \rho' = 0, \end{cases} \quad (1)$$

where $\frac{D}{Dt} = \frac{\partial}{\partial t} + \mathbf{u} \cdot \nabla$ is the material (total) derivative, Δ the Laplacian operator, ρ_0 the constant fluid density, ρ' the density perturbation in a fluid with density $\rho = \rho_0 + \rho'$ such that $\rho' \ll \rho_0$, p the pressure, ν the kinematic viscosity, κ the molecular diffusivity, \mathbf{g} the gravitational acceleration, and \mathbf{k} the unit normal vector in the vertical direction.

In LES, the large eddies are obtained by convolving the velocity \mathbf{u} with a filter function $g_\delta(\mathbf{x})$, namely $\bar{\mathbf{u}}(\mathbf{x}, t) := (g_\delta * \mathbf{u})(\mathbf{x}, t)$, and $\bar{\rho}'(\mathbf{x}, t) := (g_\delta * \rho')(\mathbf{x}, t)$. Such an averaging suppresses any fluctuations in \mathbf{u} and ρ' below the filter scale δ . The filtered Boussinesq equations read

$$\begin{cases} \frac{D\bar{\mathbf{u}}}{Dt} + \frac{1}{\rho_0} \nabla \bar{p} - \nu \Delta \bar{\mathbf{u}} + \frac{\bar{\rho}'}{\rho_0} \mathbf{g} \mathbf{k} = -\nabla \cdot \boldsymbol{\tau}(\mathbf{u}, \mathbf{u}), \\ \nabla \cdot \bar{\mathbf{u}} = 0, \\ \frac{D\bar{\rho}'}{Dt} - \kappa \Delta \bar{\rho}' = -\nabla \cdot \boldsymbol{\sigma}(\mathbf{u}, \rho'). \end{cases} \quad (2)$$

The challenge is solving the closure problem, i.e., finding appropriate models in terms of $\bar{\mathbf{u}}$ and $\bar{\rho}'$ for the *subgrid-scale stress* (SGS) tensors

$$\boldsymbol{\tau}(\mathbf{u}, \mathbf{u}) = \overline{\mathbf{u}\mathbf{u}} - \bar{\mathbf{u}} \bar{\mathbf{u}} \quad \text{and} \quad \boldsymbol{\sigma}(\mathbf{u}, \rho') = \overline{\mathbf{u} \bar{\rho}'} - \bar{\mathbf{u}} \bar{\rho}'. \quad (3)$$

Most of the SGS models that have been used for stratified geophysical flows are of eddy-viscosity type, based on developments put forth by Deardorff (1980), Pacanowski and Philander (1981), Peters et al. (1989), Schumann (1991), Métais (1998), Riley et al. (2000), Stevens and Moeng (56). Recent applications of LES to atmospheric and oceanographic problems include the studies by Wang et al. (1996), Wang et al. (1998), Raasch and Etling (1998), Skyllingstad et al. (1999), Skyllingstad and Wijesekera (2004). There are also non-eddy-viscosity SGS models, such as those proposed by Deardorff (1974), Schmidt and Schumann (1989).

Given the wide range of LES models used for stratified geophysical flows, the following natural question arises: *Which LES model performs best?* The answer to this question depends on the specific flow setting and criterion used. In this study, we investigate the ability of several different LES models to predict *mixing* in a canonical benchmark setting, the lock-exchange problem.

2.1. Eddy-viscosity LES models

The most popular approach to model the SGS tensor $\boldsymbol{\tau}(\mathbf{u}, \mathbf{u})$ is the *eddy-viscosity* (EV) model, motivated by the idea that the global effect of $\boldsymbol{\tau}(\mathbf{u}, \mathbf{u})$, in the mean, is to transfer energy from resolved to unresolved scales through inertial interactions (Frisch, 1995; Pope, 2000; Sagaut, 2006; Berselli et al., 2005). The most popular EV model is the *Smagorinsky model* (Smagorinsky, 1963), which we denote SGS-A:

$$\boldsymbol{\tau}_{\text{SGS-A}} = -2(c_s \delta)^2 |\nabla^s \bar{\mathbf{u}}| \nabla^s \bar{\mathbf{u}}, \quad \text{and} \quad \boldsymbol{\sigma}_{\text{SGS-A}} = -(c_T \delta)^2 |\nabla^s \bar{\mathbf{u}}| \nabla \bar{\rho}', \quad (4)$$

where $\nabla^s \bar{\mathbf{u}} := \frac{\nabla \bar{\mathbf{u}} + \nabla \bar{\mathbf{u}}^T}{2}$ is the deformation tensor of $\bar{\mathbf{u}}$, $|\boldsymbol{\mu}| := (2\mu_{ij}\mu_{ij})^{1/2}$ the norm of any tensor $\boldsymbol{\mu}$, c_s the Smagorinsky constant, and c_T its counterpart for $\boldsymbol{\sigma}(\mathbf{u}, \rho')$.

It is well known that the Smagorinsky constant does not have a universal value, and should be a dynamical variable. For instance, Canuto and Cheng (1997) used examples of plain strain and homogeneous shear flows to point out that c_s should be changed as a function of production and dissipation rate of turbulent kinetic energy. Several modifications of the Smagorinsky model Eq. (4) have been proposed to take into account the effect of stratification via the Richardson number $Ri = N^2/S^2$, where $N^2 = -\frac{g}{\rho_0} \frac{\partial \rho'}{\partial z}$ is the square of the buoyancy frequency, and $S^2 = (\frac{\partial u}{\partial z})^2 + (\frac{\partial v}{\partial z})^2$ is the square of vertical shear (Schumann, 1975; Stevens et al., 1998; Dörnbrack, 1998). In Özgökmen et al. (2007), we modeled unresolved anisotropic mixing in stratified fluids via splitting eddy-viscosities into horizontal and vertical components, and by regulating the vertical mixing via a function of Ri . The best results were obtained using SGS-B, in which the vertical diffusivity is Ri -dependent:

$$\begin{aligned} \boldsymbol{\tau}_{\text{SGS-B}} &= -(c_s \delta)^2 |\nabla^s \bar{\mathbf{u}}| \nabla^s \bar{\mathbf{u}}, \quad \text{and} \quad \boldsymbol{\sigma}_{\text{SGS-B}} \\ &= -\sum_{j=1}^3 [g_j(Ri)(c_T \delta)^2 |\nabla^s \bar{\mathbf{u}}| \nabla \bar{\rho}'], \end{aligned} \quad (5)$$

where $g_1(Ri) = g_2(Ri) = 1.0$ and

$$g_3(Ri) = \begin{cases} 1 & \text{for } Ri < 0, \\ \sqrt{1 - \frac{Ri}{Ri_c}} & \text{for } 0 \leq Ri \leq Ri_c, \\ 0 & \text{for } Ri > Ri_c. \end{cases} \quad (6)$$

The function $g_3(Ri)$ makes a smooth transition between 1 for $Ri < 0$ and 0 for $Ri > Ri_c$, where Ri_c is the critical threshold, typically $Ri_c = 0.25$ (Miles, 1961; Rohr et al., 1988). The rationale for this type of SGS models is that when $Ri \geq Ri_c$, shear cannot overcome stratification, and for strongly-stratified flows, mixing tends to take place primarily on the horizontal plane, or in the form of so-called “pancake mixing” (Fernando, 2000). Hence, with this modeling approach, we attempted to represent the characteristic anisotropic mixing in stratified flow. When $Ri = 0$, the motion is isotropic and the original Smagorinsky model (4) is recovered.

The *dynamic* SGS model of Germano et al. (1991) (see also Porté-Agel et al. (2000)) and the *Lagrangian dynamic* SGS model of Meneveau et al. (1996) represent major improvements of the Smagorinsky model (4). In the dynamic SGS model, the constant c_s in (4) is computed dynamically as a function of space and time:

$$c_{ds}^2 = \frac{1}{2} \frac{\langle M_{ij} L_{ij} \rangle}{\langle M_{kl} M_{kl} \rangle}. \quad (7)$$

In (7), $\langle \cdot \rangle$ denotes spanwise-averaging, and M_{ij} and L_{ij} are defined as follows:

$$M_{ij} := \tilde{\delta}^2 |\nabla^s \tilde{\mathbf{u}}| \nabla^s \tilde{u}_{ij} - \delta^2 |\nabla^s \tilde{\mathbf{u}}| \nabla^s \tilde{u}_{ij} \quad (8)$$

$$= \delta^2 \left(\alpha^2 |\nabla^s \tilde{\mathbf{u}}| \nabla^s \tilde{u}_{ij} - |\nabla^s \tilde{\mathbf{u}}| \nabla^s \tilde{u}_{ij} \right), \quad (9)$$

$$L_{ij} := \tilde{u}_i \tilde{u}_j - \tilde{u}_i \tilde{u}_j, \quad (10)$$

where a tilde denotes filtering with a test filter of radius $\tilde{\delta}$ and $\alpha := \frac{\tilde{\delta}}{\delta}$ is the filter ratio. Defining $\tilde{M}_{ij} := \frac{M_{ij}}{\delta^2}$, we can rewrite (7) as

$$c_{ds}^2 = \frac{1}{2} \frac{\langle \tilde{M}_{ij} L_{ij} \rangle}{\langle \tilde{M}_{kl} \tilde{M}_{kl} \rangle}, \quad (11)$$

which depends only on the ratio of filter widths α and has no explicit dependence on δ . Thus, replacing c_s in (4) with c_{ds} given by (11), we get the dynamic SGS model, which we denote SGS-D:

$$\begin{aligned} \tau_{\text{SGS-D}} &= -2(c_{ds}\delta)^2 |\nabla^s \tilde{\mathbf{u}}| \nabla^s \tilde{\mathbf{u}}, \quad \text{and} \\ \sigma_{\text{SGS-D}} &= -(c_{dt}\delta)^2 |\nabla^s \tilde{\mathbf{u}}| \nabla^s \tilde{\rho}', \end{aligned} \quad (12)$$

where c_{dt} is the counterpart of c_{ds} for the density perturbation SGS model. In our numerical tests, SGS-D is used with $\sigma_{\text{SGS-D}} = 0$. To ensure the positivity of (7), we use the popular clipping procedure by setting to 0 all the negative values of the right-hand side of (7) (Sagaut, 2006). Determination of the filter ratio α is relatively straightforward. For example, if one constructs a test filter that projects onto half of the number of modes, then $\alpha = 2$. With the spectral element method (Section 3), we project from the N -th-order local basis functions onto a basis of order \tilde{N} , with corresponding $\alpha = \frac{N}{\tilde{N}}$. One of the main advantages of the dynamic Smagorinsky model (12) with respect to the constant-coefficient version (4) is its ability to correctly yield $c_{ds} = 0$ in laminar regions of the flow.

It should be pointed out that there are other types of eddy-viscosity models, most notably high-pass filtered models (Stolz et al., 2005), but these models are not tested here.

2.2. Approximate deconvolution LES models

The *approximate deconvolution* (AD) models represent a promising alternative to the eddy-viscosity models (Berselli et al., 2005; John, 2004; Sagaut, 2006). Instead of using physical insight to model $\tau(\mathbf{u}, \mathbf{u})$, the AD models are developed solely on mathematical grounds. This is highly desirable in flows where the assumptions of isotropy and homogeneity (which are essential to the assumption of energy cascade) may not hold. The main idea in approximate deconvolution is to use the available numerical approximation of $\tilde{\mathbf{u}}$ to approximate \mathbf{u} .

A particular class of AD models relies on finding an approximate deconvolution of the filtered quantity by repeated filtering (Stolz and Adams, 1999), which has been shown to be an effective method for a variety of flow types, such as homogeneous transitional flows (Schlatter et al., 2004).

Another class of AD model are those obtained through wave-number asymptotics, such as the gradient (or non-linear, or tensor-diffusivity) model Leonard (1974), Clark et al. (1979), Carati et al. (2001), Winckelmans et al. (2001), Katopodes et al. (2000), Cao et al. (2005):

$$\tau(\mathbf{u}, \mathbf{u}) = \overline{\mathbf{u}\mathbf{u}} - \tilde{\mathbf{u}}\tilde{\mathbf{u}} \approx \frac{\delta^2}{2\gamma} \nabla \tilde{\mathbf{u}} \nabla \tilde{\mathbf{u}}, \quad (13)$$

where γ is a parameter in the Gaussian filter $g_\delta(\mathbf{x}) = (\frac{\delta}{\pi})^{\frac{3}{2}} \frac{1}{\delta^3} e^{-\frac{|\mathbf{x}|^2}{2\delta^2}}$ and $(\nabla \tilde{\mathbf{u}} \nabla \tilde{\mathbf{u}})_{ij} = \sum_{l=1}^3 \frac{\partial \tilde{u}_i}{\partial x_l} \frac{\partial \tilde{u}_j}{\partial x_l}$. Galdi and Layton (2000) developed the *rational LES* (RLES) model, which is an improvement of (13) based on a rational Padé approximation:

$$\tau(\mathbf{u}, \mathbf{u}) = \left[\left(\mathbb{I} - \frac{\delta^2}{4\gamma} \Delta \right)^{-1} \left(\frac{\delta^2}{2\gamma} \nabla \tilde{\mathbf{u}} \nabla \tilde{\mathbf{u}} \right) \right], \quad (14)$$

where \mathbb{I} is the identity operator. The RLES model (14) has been used in the numerical simulation of turbulent homogeneous flows (Ilie-scu and Fischer, 2003, 2004), but not for mixing in stratified flows. In this paper, we extend the RLES model to the Boussinesq equations and propose several modifications.

We start by using the convolution theorem:

$$\overline{\rho'} = \mathbf{g}_\delta * \rho' \quad \Rightarrow \quad \widehat{\rho'} = \widehat{\mathbf{g}_\delta} \widehat{\rho'} \quad \Rightarrow \quad \widehat{\rho'} = \frac{1}{\widehat{\mathbf{g}_\delta}} \widehat{\rho'} \quad \text{and} \quad \widehat{\mathbf{u}} = \frac{1}{\widehat{\mathbf{g}_\delta}} \widehat{\mathbf{u}}. \quad (15)$$

Next, we approximate $\widehat{\mathbf{g}_\delta}(\mathbf{k}) = e^{-\frac{\delta^2 \mathbf{k}^2}{4\gamma}}$, the Fourier transform of the Gaussian filter. However, instead of using a Taylor series approximation as in the derivation of the gradient model (13), we follow Galdi and Layton (2000) and use a (0,1) rational Padé approximation:

$$\widehat{\mathbf{g}_\delta}(\mathbf{k}) = e^{-\frac{\delta^2 \mathbf{k}^2}{4\gamma}} = \frac{1}{1 + \frac{\delta^2 \mathbf{k}^2}{4\gamma}} + \mathcal{O}(\delta^4). \quad (16)$$

The approximation (16) has the same (formal) order of accuracy with respect to δ as a Taylor series approximation, but preserves the decay of the high wave number components in $\widehat{\mathbf{g}_\delta}$, whereas the Taylor series approximation actually *increases* the high wave number components. For the inverse of the Fourier transform of the Gaussian filter, however, the Taylor approximation is appropriate.

$$\frac{1}{\widehat{\mathbf{g}_\delta}(\mathbf{k})} = e^{\frac{\delta^2 \mathbf{k}^2}{4\gamma}} = 1 + \frac{\delta^2 |\mathbf{k}|^2}{4\gamma} + \mathcal{O}(\delta^4). \quad (17)$$

Thus, by using (17) in (15), dropping all terms formally of order $\mathcal{O}(\delta^4)$ and higher, and taking the inverse Fourier transform, we get

$$\rho' \approx \overline{\rho'} - \frac{\delta^2}{4\gamma} \Delta \overline{\rho'} \quad \text{and} \quad \mathbf{u} \approx \tilde{\mathbf{u}} - \frac{\delta^2}{4\gamma} \Delta \tilde{\mathbf{u}} \quad \text{implying} \quad (18)$$

$$\begin{aligned} \mathbf{u}\rho' &= \overline{\mathbf{u}\rho'} - \frac{\delta^2}{4\gamma} (\tilde{\mathbf{u}} \Delta \overline{\rho'} + \overline{\rho'} \Delta \tilde{\mathbf{u}}) + \mathcal{O}(\delta^4) \\ &= \overline{\mathbf{u}\rho'} - \frac{\delta^2}{4\gamma} \Delta (\overline{\mathbf{u}\rho'}) + \frac{\delta^2}{2\gamma} \nabla \tilde{\mathbf{u}} \nabla \overline{\rho'} + \mathcal{O}(\delta^4), \end{aligned} \quad (19)$$

where $(\nabla \tilde{\mathbf{u}} \nabla \overline{\rho'})_i = \sum_{l=1}^3 \frac{\partial \tilde{u}_i}{\partial x_l} \frac{\partial \overline{\rho'}}{\partial x_l}$. By taking the Fourier transform of (19), using the rational Padé approximation (16), and then taking the inverse Fourier transform, we get

$$\begin{aligned} \overline{\mathbf{u}\rho'} &= \left(\mathbb{I} - \frac{\delta^2}{4\gamma} \Delta \right)^{-1} \left[\left(\mathbb{I} - \frac{\delta^2}{4\gamma} \Delta \right) \overline{\mathbf{u}\rho'} + \frac{\delta^2}{2\gamma} \nabla \mathbf{u} \nabla \rho' \right] + \mathcal{O}(\delta^4) \\ &= \overline{\mathbf{u}\rho'} + \left(\mathbb{I} - \frac{\delta^2}{4\gamma} \Delta \right)^{-1} \left(\frac{\delta^2}{2\gamma} \nabla \mathbf{u} \nabla \rho' \right) + \mathcal{O}(\delta^4). \end{aligned} \quad (20)$$

Thus, dropping all terms formally of order $\mathcal{O}(\delta^4)$ and higher in (20), we get

$$\boldsymbol{\sigma}(\mathbf{u}, \rho') = \overline{\mathbf{u}\rho'} - \overline{\mathbf{u}\rho'} \approx \left(\mathbb{I} - \frac{\delta^2}{4\gamma} \Delta \right)^{-1} \left(\frac{\delta^2}{2\gamma} \nabla \mathbf{u} \nabla \rho' \right). \quad (21)$$

Replacing the stress tensors $\boldsymbol{\sigma}(\mathbf{u}, \rho')$ (21) and $\boldsymbol{\tau}(\mathbf{u}, \mathbf{u})$ (14) in the filtered Boussinesq equations (2), yields the *Rational LES model for the Boussinesq equations*, denoted SGS-R:

$$\begin{aligned} \boldsymbol{\tau}_{\text{SGS-R}} &= \left(-\frac{\delta^2}{4\gamma} \Delta + \mathbb{I} \right)^{-1} \left(\frac{\delta^2}{2\gamma} \nabla \mathbf{u} \nabla \mathbf{u} \right), \quad \text{and} \\ \boldsymbol{\sigma}_{\text{SGS-R}} &= \left(-\frac{\delta^2}{4\gamma} \Delta + \mathbb{I} \right)^{-1} \left(\frac{\delta^2}{2\gamma} \nabla \mathbf{u} \nabla \rho' \right). \end{aligned} \quad (22)$$

The SGS-R model poses several challenges. The first is the specification of boundary conditions for the Helmholtz problem in computing $\boldsymbol{\sigma}$ and $\boldsymbol{\tau}$. Since $\delta \rightarrow 0$ near the boundary (Section 4), the filtering operation becomes multiplication by the identity operator. Thus, we chose homogeneous Dirichlet boundary conditions for $\boldsymbol{\sigma}$ (and similarly for $\boldsymbol{\tau}$):

$$\begin{cases} \left(\mathbb{I} - \frac{\delta^2}{4\gamma} \Delta \right) \boldsymbol{\sigma} = \frac{\delta^2}{2\gamma} \nabla \mathbf{u} \nabla \rho' & \text{in } \Omega \\ \boldsymbol{\sigma} = 0 & \text{on } \partial\Omega. \end{cases} \quad (23)$$

Other challenges are development of efficient discretizations of (23) and finding optimal scalings between the LES parameters in $\boldsymbol{\tau}$ and $\boldsymbol{\sigma}$. These are discussed in detail in Section 5.2.

2.3. Mixed and hybrid LES models

In order to explore the importance of $\boldsymbol{\sigma}$ in improving the performance of the LES, several steps are taken. These steps include a mixed model, denoted model SGS-M, in which we employed SGS-R for the momentum equation and SGS-B in the density perturbation equation:

$$\begin{aligned} \boldsymbol{\tau}_{\text{SGS-M}} &= \left(-\frac{\delta^2}{4\gamma} \Delta + \mathbb{I} \right)^{-1} \left(\frac{\delta^2}{2\gamma} \nabla \mathbf{u} \nabla \mathbf{u} \right), \quad \text{and} \\ \boldsymbol{\sigma}_{\text{SGS-M}} &= \sum_{j=1}^3 \left[\mathbf{g}_j(Ri) (c_T \delta)^2 |\nabla^s \mathbf{u}| \nabla \rho' \right]. \end{aligned} \quad (24)$$

Table 1
List of the SGS models investigated in this study.

Smagorinsky model SGS-A	$\boldsymbol{\tau}_{\text{SGS-A}} = -2(c_s \delta)^2 \nabla^s \mathbf{u} \nabla^s \mathbf{u}$, $\boldsymbol{\sigma}_{\text{SGS-A}} = -(c_T \delta)^2 \nabla^s \mathbf{u} \nabla \rho'$, where c_s and c_T are specified.
Ri-dependent Smagorinsky model SGS-B	$\boldsymbol{\tau}_{\text{SGS-B}} = -2(c_s \delta)^2 \nabla^s \mathbf{u} \nabla^s \mathbf{u}$, $\boldsymbol{\sigma}_{\text{SGS-B}} = -\sum_{j=1}^3 \left[\mathbf{g}_j(Ri) (c_T \delta)^2 \nabla^s \mathbf{u} \nabla \rho' \right]$. where $\mathbf{g}_j(Ri)$ is given in (6).
Dynamic Smagorinsky model SGS-D	$\boldsymbol{\tau}_{\text{SGS-D}} = -2(c_{ds} \delta)^2 \nabla^s \mathbf{u} \nabla^s \mathbf{u}$ $\boldsymbol{\sigma}_{\text{SGS-D}} = 0$, where c_{ds} is computed from (9)–(11).
Rational model SGS-R	$\boldsymbol{\tau}_{\text{SGS-R}} = \left(-\frac{\delta^2}{4\gamma} \Delta + \mathbb{I} \right)^{-1} \left(\frac{\delta^2}{2\gamma} \nabla \mathbf{u} \nabla \mathbf{u} \right)$, $\boldsymbol{\sigma}_{\text{SGS-R}} = \left(-\frac{\delta^2}{4\gamma} \Delta + \mathbb{I} \right)^{-1} \left(\frac{\delta^2}{2\gamma} \nabla \mathbf{u} \nabla \rho' \right)$
Mixed model SGS-M	$\boldsymbol{\tau}_{\text{SGS-M}} = \left(-\frac{\delta^2}{4\gamma} \Delta + \mathbb{I} \right)^{-1} \left(\frac{\delta^2}{2\gamma} \nabla \mathbf{u} \nabla \mathbf{u} \right)$, $\boldsymbol{\sigma}_{\text{SGS-M}} = \sum_{j=1}^3 \left[\mathbf{g}_j(Ri) (c_T \delta)^2 \nabla^s \mathbf{u} \nabla \rho' \right]$.
Hybrid model SGS-H	$\boldsymbol{\tau}_{\text{SGS-H}} = \left(-\frac{\delta^2}{4\gamma} \Delta + \mathbb{I} \right)^{-1} \left(\frac{\delta^2}{2\gamma} \nabla \mathbf{u} \nabla \mathbf{u} \right) - 2(c_{ds} \delta)^2 \nabla^s \mathbf{u} \nabla^s \mathbf{u}$, $\boldsymbol{\sigma}_{\text{SGS-H}} = 0$.

Finally, and most importantly, a hybrid model is constructed in an attempt to combine the energy cascade and dissipation characteristics of the dynamic Smagorinsky model with the ability of the rational model to preserve high wave number components of the flow field. This model is denoted SGS-H, and consists only of the following momentum stress tensor:

$$\boldsymbol{\tau}_{\text{SGS-H}} = \left(-\frac{\delta^2}{4\gamma} \Delta + \mathbb{I} \right)^{-1} \left(\frac{\delta^2}{2\gamma} \nabla \mathbf{u} \nabla \mathbf{u} \right) - 2(c_{ds} \delta)^2 |\nabla^s \mathbf{u}| \nabla^s \mathbf{u}. \quad (25)$$

In SGS-H, $\boldsymbol{\sigma}_{\text{SGS-H}} = 0$ for reasons that will become apparent in Section 5.2. A similar hybrid model, combining the gradient model (13) and the dynamic model (12) has been used in Winckelmans et al. (2001).

For convenience, the SGS models are listed in Table 1.

3. Numerical model

For all the numerical experiments in this paper, we used Nek5000. This code is based on the spectral element method (Patera, 1984; Maday and Patera, 1989; Fischer, 1997), which combines the high-order accuracy of spectral methods with the geometric flexibility of traditional finite-element methods. Spectral element discretizations have also been used in the DNS of the lock-exchange problem (Cantero et al., 2007; Härtel et al., 2000).

The time advancement of the Boussinesq equations (1) is based on second-order semi-implicit operator-splitting methods (Maday et al., 1990; Fischer, 1997). The hydrodynamics are advanced first, with explicit treatment of the buoyancy forcing term, followed by the update of the density perturbation transport. Spatial discretization is based on the spectral element method, which is a high-order weighted residual technique based on compatible velocity and pressure spaces free of spurious modes. Locally, the spectral element mesh is structured, with the solution, data, and geometry expressed as sums of N th-order Lagrange polynomials on tensor-products of Gauss–Lobatto–Legendre (GLL) quadrature points. Globally, the mesh is an unstructured array of K deformed hexahedral elements and can include geometrically non-conforming elements. For problems having smooth solutions, the spectral element method achieves exponential convergence with N , despite having only C^0 continuity (which is advantageous for parallelism). The convection operator exhibits minimal numerical dissipation and dispersion, which is critical for high Reynolds number applications. For the sparse linear solvers, Nek5000 employs as a preconditioner the additive overlapping Schwarz method (Dryja et al., 1987; Fischer and Ronquist, 1994; Fischer, 1997; Fischer and Gottlieb, 1997; Lottes and Fischer, 2005), which uses fast local solvers that exploit the tensor-product form and a parallel coarse-grid solver that scales to thousands of processors (Tufo and Fischer, 2001).

For high Reynolds number flows, Nek5000 employs two methods to achieve numerical stability without compromising the solution accuracy. The first method is dealiasing through the 3/2 rule (Deville et al., 2002). The second method, first proposed by Fischer and Mullen (2001), is polynomial filtering, in which the amplitude of the highest order basis polynomial is reduced by a β fraction. This will dampen high-frequency oscillations and reduce the accumulation of energy in the highest wave numbers by transferring the β fraction of the energy over to the third-highest order polynomial. In the present study, all computations are carried out with dealiasing and using 5% filtering ($\beta = 0.05$).

Nek5000 has also been used in the numerical investigation of various LES models, both of eddy-viscosity and approximate deconvolution type (Iliescu and Fischer, 2003, 2004). It has been used in the numerical simulation of homogeneous flows, such as the turbulent channel flow (Iliescu and Fischer, 2003, 2004), as well as stratified flows, such as the 2D lock-exchange problem

(Özgökmen et al., 2007). Finally, Nek5000 has been used in the numerical simulation of bottom gravity currents (Özgökmen et al., 2004a,b, 2006; Özgökmen and Fischer, 2008), and these results have been subsequently used to refine parameterizations of gravity current mixing for an ocean general circulation model (Chang et al., 2005; Xu et al., 2006).

4. Model configuration and parameters

The computational domain is $-\frac{L}{2} \leq x \leq \frac{L}{2}$, $0 \leq y \leq W$, and $0 \leq z \leq H$, where $L/H = 5$ and $W/H = 1$. At the top, bottom, left and right boundaries, no-flow and free-slip boundary conditions are used for the velocity components, while no-flux (insulation) conditions are used for the density perturbation ρ' :

$$\frac{\partial u}{\partial \mathbf{n}} = 0; \quad \frac{\partial w}{\partial \mathbf{n}} = 0; \quad (u, v, w) \cdot \mathbf{n} = 0; \quad \frac{\partial \rho'}{\partial \mathbf{n}} = 0, \quad (26)$$

where \mathbf{n} is the normal to the boundary. In the spanwise direction, periodic boundary conditions are used both for velocity and density perturbation fields.

$$v(x, 0, z) = v(x, W, z); \quad \rho'(x, 0, z) = \rho'(x, W, z). \quad (27)$$

Similar boundary conditions were used in the DNS of lock-exchange problem by Cantero et al. (2007) and Härtel et al. (2000).

In order to initialize the lock-exchange problem, dense fluid on the left is separated from the light fluid on the right by a sharp transition layer:

$$\frac{\rho'(x, y, z, 0)}{\Delta \rho'} = \begin{cases} 1 & \text{for } -0.5L \leq x < -(0.005 + \eta)L, \\ 100(0.005 - \frac{x}{L} - \eta) & \text{for } -(0.005 + \eta)L \leq x < +(0.005 - \eta)L, \\ 0 & \text{for } +(0.005 - \eta)L \leq x \leq +0.5L. \end{cases} \quad (28)$$

The perturbation superimposed on the density interface in order to facilitate transition to 3D flows (Fig. 1a) is $\eta = 0.05 \sin(2\pi \frac{y}{W})$. In our numerical experiments, we noticed that in the absence of this perturbation, the system lacked any span-wise asymmetries in the domain geometry, boundary conditions or forcing, and the flow maintained a perfectly 2D character well into the simulation. Similar initial perturbations were used in the DNS of lock-exchange problem by Cantero et al. (2007) and Härtel et al. (2000). Since the tilting of the density interface puts the system gradually into motion, the system is started from a state of rest, $\mathbf{u} = 0$.

The system is integrated until the rate of stratified mixing becomes small with respect to the initial vigorous activity. An important time scale in this system is the time it takes for the gravity currents to reach the walls on either side of the domain. It is found that many successive encounters of the gravity currents with the walls are required before the mixing regime subsides and the motion is primarily dominated by linear (non-mixing) internal waves. The integration time T corresponds to approximately nine encounters of the gravity current front with the walls at $x = -L/2$ and $x = L/2$. One of the inherent time scales in the system is the

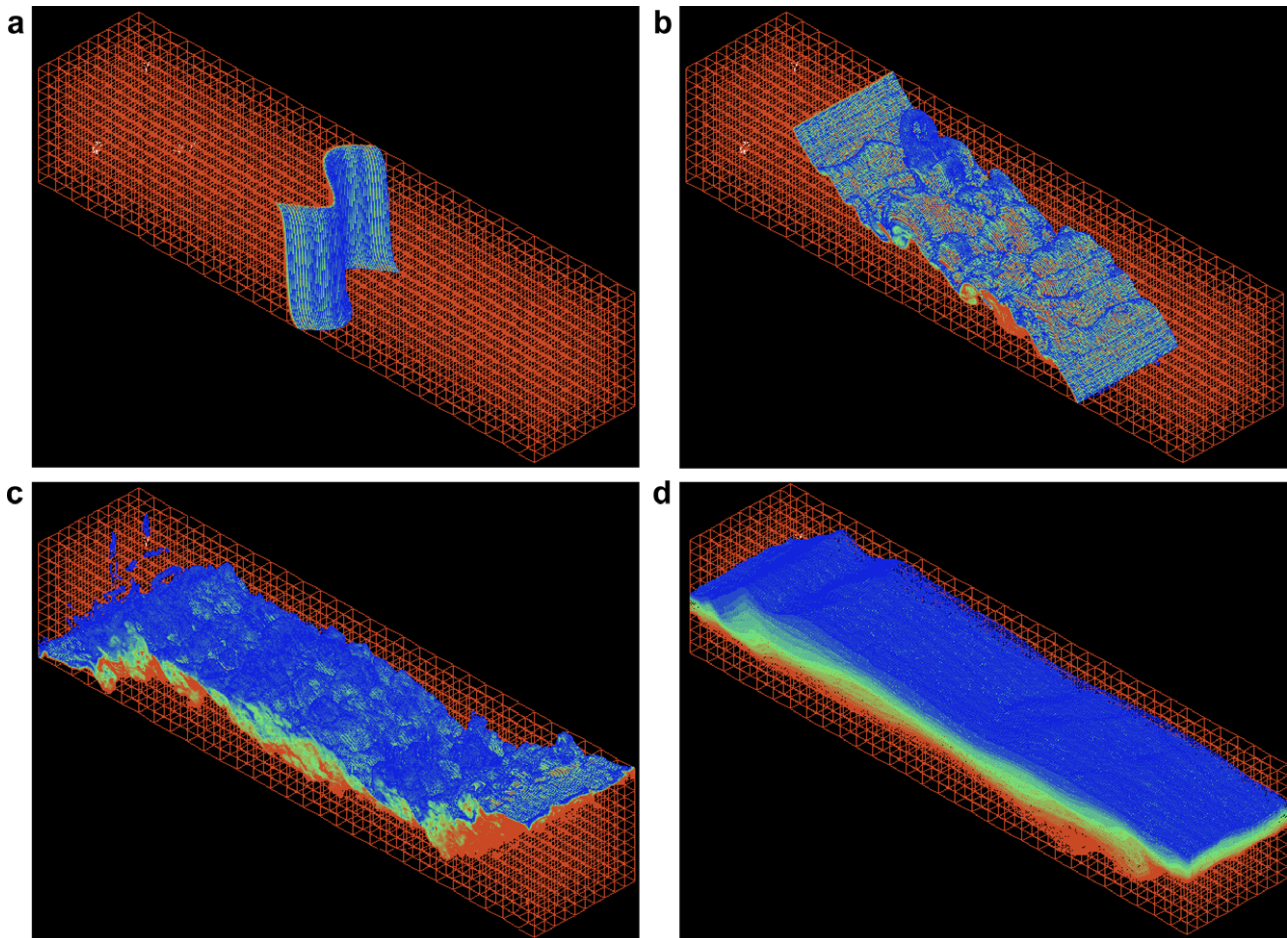


Fig. 1. Distribution of the density perturbation $\rho'(x, y, z, t)/\rho_0$ at (a) $t = 0$, (b) $t/T_b = 0.46$, (c) $t/T_b = 1.38$, and (d) $t/T_b = 19.1$ in high-res DNS. The animation of this simulation can be downloaded from: <http://www.rsmas.miami.edu/personal/tamay/3D/DNS-3d-highres.gif>.

buoyancy period $T_b = 2\pi N_\infty^{-1}$, where $N_\infty = \sqrt{\frac{g}{\rho_0} \frac{\Delta\rho'}{H}}$ is the buoyancy frequency based on the density difference over the total vertical extent H of the system. The total integration period T needs to be much larger than T_b for the effects of stratification to fully develop. In this study, integrations are terminated at $T/T_b \approx 19$.

The model parameters are determined by non-dimensionalizing the Boussinesq equations (1) using $\mathbf{u} = U_0 \mathbf{u}^*$, $\mathbf{x} = \ell \mathbf{x}^*$, $t = \frac{\ell}{U_0} t^*$, $p = \rho_0 U_0^2 p^*$, $\rho' = \Delta\rho' \rho^*$, where U_0 and ℓ are characteristic speed and length scales of the problem, and $\Delta\rho'$ is the density difference between the two main water masses. Here, U_0 will be taken as the initial gravity current speed (defined below) and $\ell = H/2$ the average thickness of the two counter-propagating gravity currents. Dropping “*” for non-dimensional variables, yields

$$\begin{cases} \frac{D\mathbf{u}}{Dt} + \nabla p - \frac{1}{Re} \Delta \mathbf{u} + \frac{1}{Pr^2} \rho' \mathbf{k} = \mathbf{0} \\ \nabla \cdot \mathbf{u} = 0 \\ \frac{D\rho'}{Dt} - \frac{1}{RePr} \Delta \rho' = 0, \end{cases} \quad (29)$$

where the non-dimensional parameters are the Reynolds number $Re = U_0 \ell / \nu$, the Prandtl number $Pr = \nu / \kappa$, and the Froude number $Fr = U_0 / \sqrt{g \Delta\rho' \ell / \rho_0}$, which is the ratio between the characteristic advection speed and the internal wave speed. In the case of the lock-exchange problem, U_0 is given by $U_0 = \sqrt{g \Delta\rho' \ell (H - \ell) / (\rho_0 H)}$, and since $\ell = H/2$ here, the initial gravity current speed is well approximated by $U_0 = \frac{1}{2} \sqrt{g \Delta\rho' H / \rho_0}$. Therefore, the Froude number is set to $Fr = 2^{-1/2}$. As such, a weakly-stratified flow regime is to be expected, in which overturns can readily take place, as opposed to layer formation in the strongly-stratified regime, $Fr \ll 1$. The Prandtl number is taken as $Pr = 7$, which corresponds to that of heat and water at room temperature. The primary free parameter of this system is Re . Here, we set $Re = 3000$.

The spatial resolutions used in the numerical experiments are summarized in Table 2. The highest resolution computation (denoted high-res) is carried out using $K_x = 48$, $K_y = 16$, $K_z = 16$ elements in x, y, z directions, respectively (the total number of elements being $K = K_x K_y K_z = 12,288$), with a polynomial of order $N = 13$ in each direction, corresponding to $n = 27,300,625$ spatial points. With this resolution, $T/T_b = 19$ is achieved in $m = 250,000$ time steps while maintaining the Courant number to be less than 0.5. The CPU time requirement was 30 days using $P = 128$ proces-

sors on Virginia Tech's SystemX (www.tcf.vt.edu). Since the results for high-res did not differ significantly from med-res2 DNS* and only little with respect to med-res1 DNS*, we concluded that grid convergence was achieved. Then, a series of coarse-resolution simulations are conducted, so-called low-res1, low-res2 and low-res3, by reducing both the number of elements and the spectral order, and by increasing the time step so that they are 2292–14,864-fold faster than the DNS.

The parameters of the SGS models are listed in Table 3. The classic Smagorinsky model SGS-A is tested with $c_s = 0.05$ and $c_s = 0.10$, which seem to cover the conventional parameter regime (Ferziger, 2005). For simplicity, we first set $c_T = c_s$. Noting that $Pr = 7$ implies smaller turbulent features in the density perturbation field than in the velocity field, we also experiment with $c_T < c_s$, or specifically set $c_s = 0.05$ and $c_T = 0.01$. Effectively, this is equivalent to using a smaller filter size for the density perturbation field, as the SGS stresses (4), (5) involve a proportionality constant of $(c_T \delta)^2$. The Ri -dependent version SGS-B introduced in Özgökmen et al. (2007) is also tested with the same c_s and c_T parameter combinations, and with $Ri_c = 0.25$. Three sets of test filter ratios are used for the dynamic Smagorinsky model SGS-D, namely $\alpha = N/(N - 1)$, which corresponds to $\alpha = 1.2$ for low-res1 and low-res2 and to $\alpha = 1.14$ for low-res3, and $\alpha = N/(N - 2)$ corresponding to $\alpha = 1.5$ for low-res1 and low-res2 and to $\alpha = 1.33$ for low-res3. We cover a wider parameter range for low-res3 by adding $\alpha = N/(N - 3) = 1.6$. The parameter selections for the rational model SGS-R, mixed and hybrid models (SGS-M and SGS-H) are discussed in Section 5.2.

The filter radius δ is taken as

$$\delta(x, y, z) = \delta_0 \left\{ 1 - \left[\exp\left(-\frac{x + \frac{1}{2}}{\epsilon}\right) \right]^2 \right\} \left\{ 1 - \left[\exp\left(-\frac{x - \frac{1}{2}}{\epsilon}\right) \right]^2 \right\} \times \left\{ 1 - \left[\exp\left(-\frac{z}{\epsilon}\right) \right]^2 \right\} \left\{ 1 - \left[\exp\left(-\frac{z - H}{\epsilon}\right) \right]^2 \right\}, \quad (30)$$

where $\delta_0 = (\Delta_x^m \Delta_y^m \Delta_z^m)^{1/3}$ and Δ_x^m , Δ_y^m , and Δ_z^m are the largest spaces between GLL points in each hexahedral element in x, y , and z directions, respectively. The role of the four factors multiplying δ_0 in (30) is to make δ approach 0 near solid walls, that is, to effect the damping near the walls. Note that this damping acts only in the x and z

Table 2

Table of the spatial resolutions used for DNS* and DNS. DNS* denotes under-resolved simulations without SGS stress models. The number of grid points is $n = (K_x N + 1)(K_y N + 1)(K_z N + 1)$, where N is the polynomial degree, K_x , K_y , and K_z are the number of elements in x, y, z directions, respectively. The computation (CPU) time is approximately proportional to mKN^4 , where m is the number of time steps. Wall-clock time is CPU time divided by the number of processors P . The computational gain factor with respect to DNS is listed. Experiments denoted med-res2 DNS* and high-res DNS are run on Virginia Tech's SystemX, based on 2000 Apple G5 processors with a clock speed of 2.3 GHz, whereas most of the remaining experiments are completed on 8–16 processor clusters based on 2.6 GHz dual-core Opteron chips at the University of Miami. All systems have a similar performance in the parallel environment.

Exp	Resolution	m	P	CPU hours	Computational gain wrt DNS
DNS*	low-res1 $K = 12 \times 4 \times 4 = 192$; $N = 6$ $n = 45,625$	25,000	4	6.2	14,864
DNS*	low-res2 $K = 15 \times 5 \times 5 = 375$; $N = 6$ $n = 87,451$	25,000	4	17.0	5421
DNS*	low-res3 $K = 375$; $N = 8$; $n = 203,401$	25,000	4	40.2	2292
DNS*	med-res1 $K = 30 \times 10 \times 10 = 3000$; $N = 12$ $n = 5,285,401$	75,000	8	5519.7	17
DNS*	med-res2 $K = 48 \times 16 \times 16 = 12,288$; $N = 9$ $n = 9,103,825$	66,666	64	7670.7	12
DNS	high-res $K = 12,288$; $N = 13$; $n = 27,300,625$	250,000	128	92,160.0	1

Table 3

Parameters of the LES models used in this study. SGS-A refers to the classic Smagorinsky model, SGS-B is the Ri -dependent Smagorinsky model, SGS-D is the dynamic Smagorinsky model, SGS-R is the RLES model, SGS-M is the mixed case, where SGS-R is used in the momentum equations and SGS-B in the density perturbation transport equation, and SGS-H is the hybrid case, where the combination of the dynamic Smagorinsky and the RLES models is used as momentum stress tensors.

SGS-A	$c_s = c_T = 0.05$ $c_s = c_T = 0.10$ $c_s = 0.05, c_T = 0.01$
SGS-B	$c_s = c_T = 0.05, Ri_c = 0.25$ $c_s = c_T = 0.10, Ri_c = 0.25$ $c_s = 0.05, c_T = 0.01, Ri_c = 0.25$
SGS-D	$\alpha = N/(N-1)$ $\alpha = N/(N-2)$ $\alpha = N/(N-3)$ $1.14 \leq \alpha \leq 1.6$
SGS-R	$\gamma = 6, \gamma_T = 6$ $\gamma = 3, \gamma_T = 10$ $\gamma = 1.5, \gamma_T = 12$ $\gamma = 1, \gamma_T = 15$
SGS-M	$\gamma = 1.5, c_T = 0.10, Ri_c = 0.25$ $\gamma = 1.5, c_T = 0.01, Ri_c = 0.25$ $\gamma = 1.5, \sigma = 0$
SGS-H	$\gamma = 1, \alpha = N/(N-1)$ or $\alpha = N/(N-2)$

directions, since the y direction corresponds to periodic boundary conditions. The need for damping in LES near solid walls, especially for eddy-viscosity models, is well documented (Sagaut, 2006; Pope,

2000; Berselli et al., 2005). The damping usually addresses two issues concerning LES near solid walls: first, the SGS stresses should have the correct physical behavior (i.e., follow the boundary layer theory). Second, the numerical discretization of the SGS stresses should be stable. Since the physical insight used in classic engineering flows is not available in our setting, we thus focus on the numerical stability of the SGS stresses. The parameter ϵ controls the distance from solid walls over which δ decays to zero. For SGS-A and SGS-B models, it is found that ϵ neither has an impact on results, nor creates any numerical instabilities, provided that it is small. It is set to $\epsilon = 0.01$ in most simulations. However, in the case of SGS-R, clear deviations of the density perturbation fields from the DNS solution near the solid boundaries and subsequent numerical instabilities are encountered for $\epsilon = 0.01$. These problems disappear for larger values of ϵ and an optimal value appears to be around $\epsilon = 0.12$. In order to make a fair comparison with other LES models, $\epsilon = 0.12$ is used for a set of experiments with SGS-B as well.

The selection of boundary conditions is one of the outstanding challenges in LES. There are currently two types of LES boundary conditions (Pope, 2000): *Near Wall Resolution (NWR)* and *Near Wall Modeling (NWM)*. In NWR, the filter radius δ is variable and shrinks to 0 as we approach the boundary. In NWM, the filter radius δ is kept constant near the boundary. Since the focus of this paper is on developing appropriate SGS models (and not boundary conditions) for mixing in stratified flows, we decided to simply choose the more popular NWR approach: $\delta = \delta(x, y, z) \rightarrow 0$ near the solid walls (see (30)). Indeed, although more expensive computationally, the NWR does not require the additional physical insight needed in

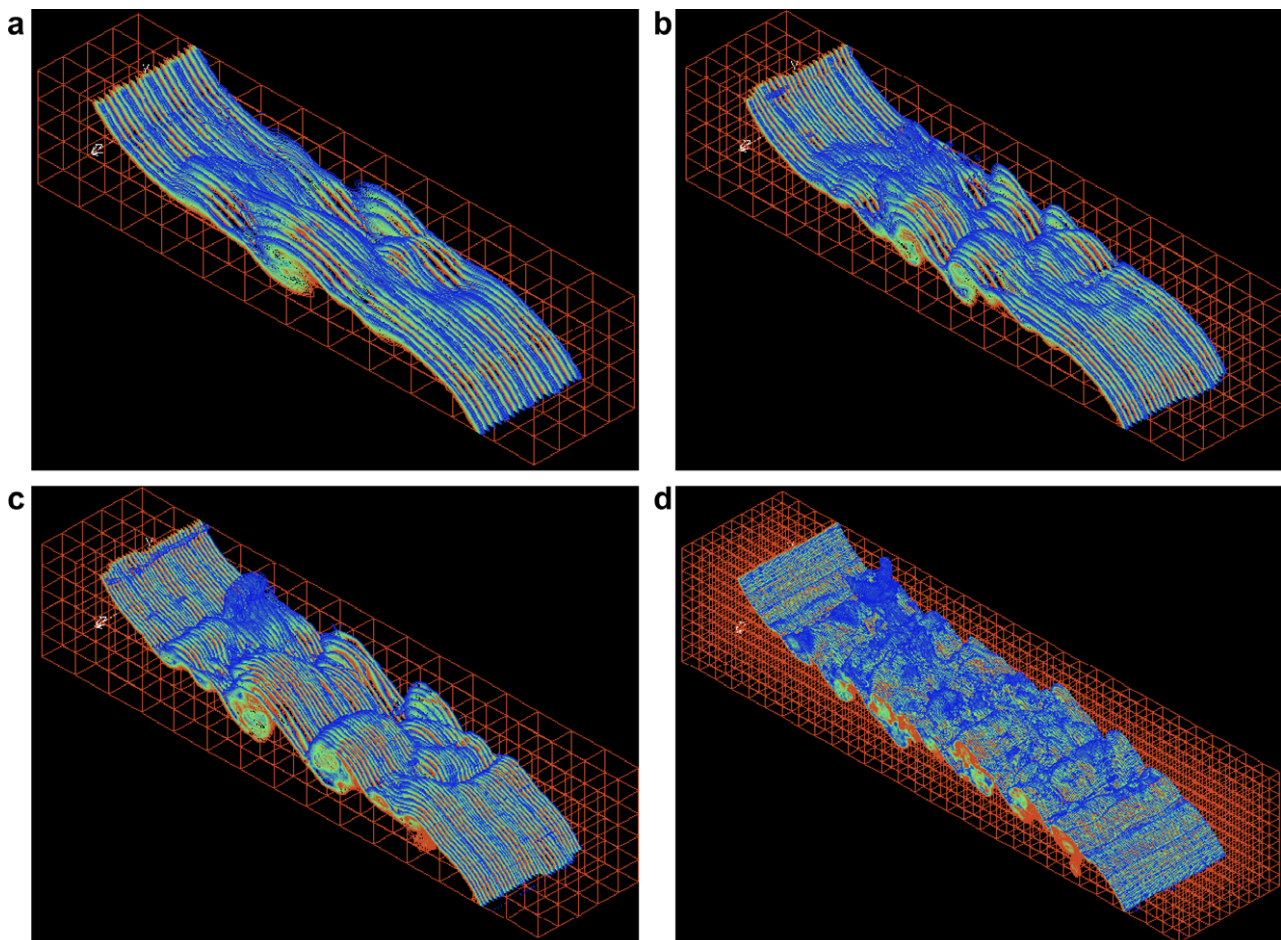


Fig. 2. Distributions of the density perturbation $\rho(x, y, z, t)/\rho_0$ at $t/T_b = 0.61$ for (a) low-res1 DNS*, (b) low-res2 DNS*, (c) low-res3 DNS*, (d) high-res DNS.

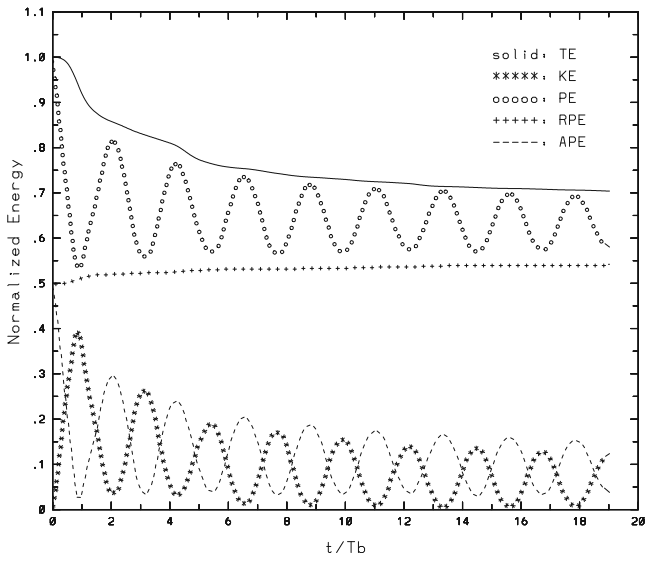


Fig. 3. Time evolutions of volume averaged total energy TE, potential energy PE, kinetic energy KE, available potential energy APE and background potential energy RPE, normalized by $PE_0 = \frac{1}{4} g \Delta \rho' L H^2 W$ from high-res DNS.

NWM, which is generally not available in oceanic flows. Since $\delta \rightarrow 0$ near the boundary, the filtered variables approach the unfiltered variables $\bar{u} \rightarrow u$; $\bar{v} \rightarrow v$; $\bar{w} \rightarrow w$; $\bar{\rho}' \rightarrow \rho'$. Thus, for the SGS

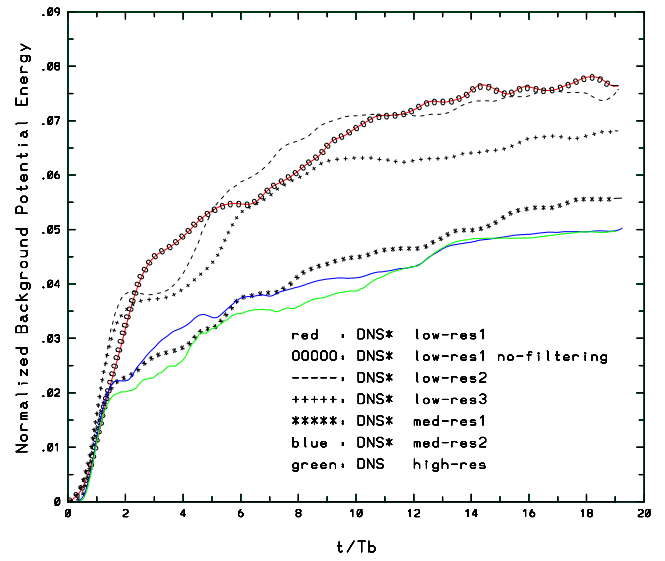


Fig. 4. Time evolution of the normalized background potential energy $RPE'(t)$, in DNS with different resolutions.

models, we used the same boundary conditions as those used for the DNS (26,27):

$$\frac{\partial \bar{u}}{\partial \mathbf{n}} = 0; \quad \frac{\partial \bar{w}}{\partial \mathbf{n}} = 0; \quad (\bar{u}, \bar{v}, \bar{w}) \cdot \mathbf{n} = 0; \quad \frac{\partial \bar{\rho}'}{\partial \mathbf{n}} = 0, \quad (31)$$

$$\bar{v}(x, 0, z) = \bar{v}(x, W, z); \quad \bar{\rho}'(x, 0, z) = \bar{\rho}'(x, W, z). \quad (32)$$

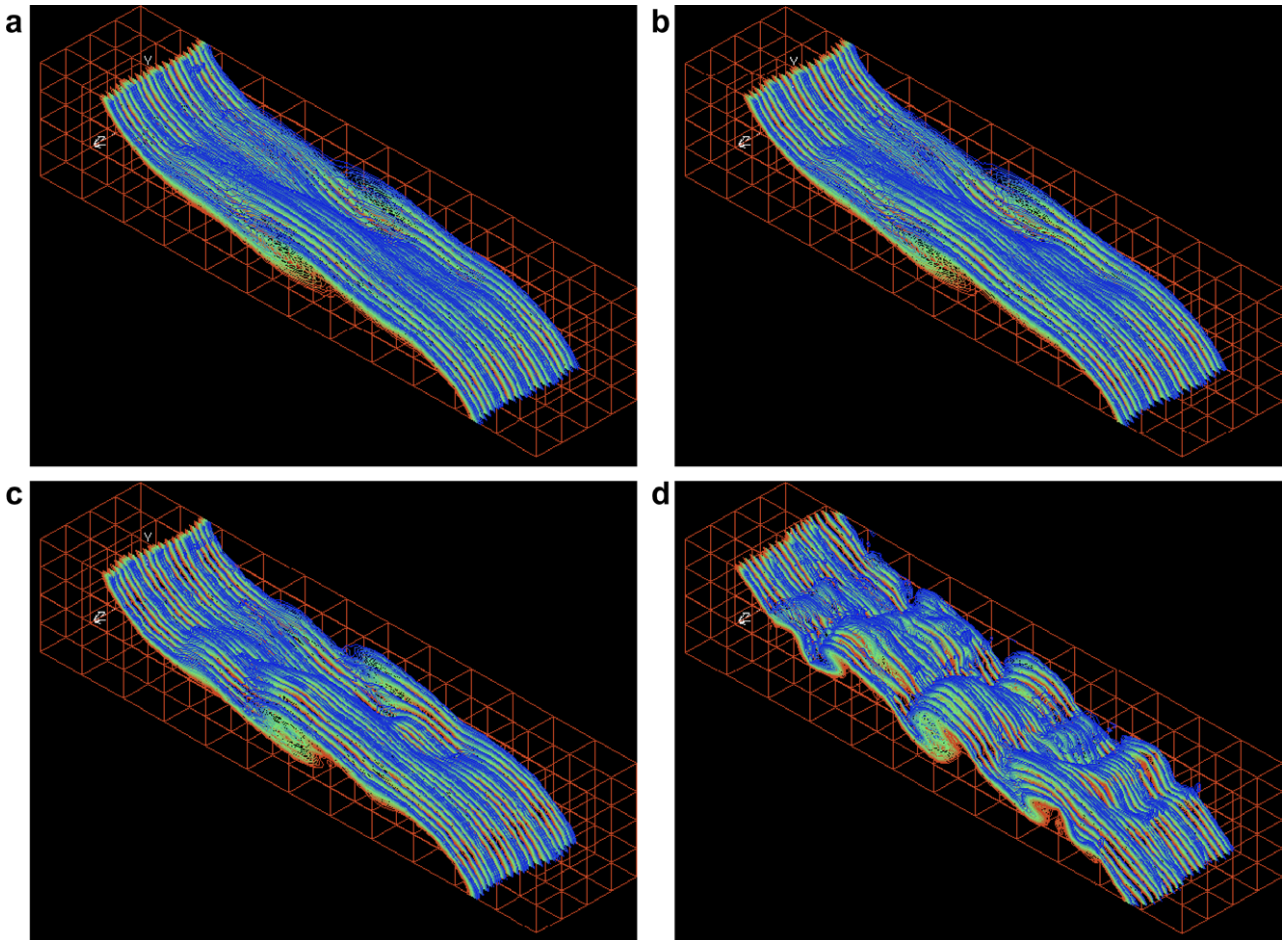


Fig. 5. Density perturbation field $\rho'(x,y,z,t)/\rho_0$ at $t/T_b = 0.61$ from low-res1 LES using (a) SGS-A with $c_s = c_T = 0.10$, (b) SGS-B with $c_s = c_T = 0.10$ and $Ri_c = 0.25$, (c) SGS-D with $\alpha = 1.2$, and (d) SGS-R with $\gamma = 1$ and $\gamma_T = 15$.

5. Results

This section presents results from numerical experiments with the six LES models considered in this paper: (i) the classic Smagorinsky model SGS-A (4); (ii) the Smagorinsky model with Ri -dependent diffusivity SGS-B (5); (iii) the dynamic Smagorinsky model SGS-D (12); (iv) the rational LES model SGS-R (22); (v) the mixed model SGS-M (24); and (vi) the hybrid model SGS-H (25). We perform a thorough *a posteriori* testing of all six LES models on three coarse meshes. That is, we first perform a DNS (Section 5.1) on a fine mesh, and then perform LES (Section 5.2) on the coarse meshes. The closer the LES results are to the DNS results, the better the LES model is. To decouple the numerical effects from the LES modeling effects, we also run a DNS*, which is a numerical simulation without an SGS model on the same coarse mesh used for the LES models. Thus, any relevant LES simulation should satisfy two minimal requirements: (i) yield better results than DNS*; and (ii) have a computational cost similar to that of DNS*.

5.1. DNS results

5.1.1. Description

To determine the achievement of DNS spatial resolution, we monitor the time evolution of background potential energy as a function of the spatial resolution. This process, which is described in detail in Section 5.1.2, yields high-res DNS (see Table 2) as the DNS resolution. Thus, in the sequel, we will refer to high-res DNS

as DNS. Similar spatial resolutions were used in the DNS of lock-exchange problem by Cantero et al. (2007) and Härtel et al. (2000).

The time evolution of the density perturbation field from high-res DNS is depicted at selected instants in Fig. 1b–d. Once the density interface starts tilting, it generates two counter-propagating gravity currents (Simpson, 1987) and the shear across the interface leads to instabilities. The initial instability is in the form of 2D Kelvin–Helmholtz (KH) rolls, which constitute the usual first step toward the onset of more complex mixing of the density field. Later on, coherent structures of the form of hair-pin vortices are also visible (Fig. 1b). As an active tracer, the density perturbation field carries Lagrangian characteristics. Therefore, it is a natural and practical substitute to Q -criterion (Hunt et al., 1988), which is used to locate regions where rotation dominates the strain in the flow field, or to direct Lyapunov exponents that rely on the separation on Lagrangian particle pairs released in the flow field in order to visualize the turbulent coherent structures (Green et al., 2007). The initial 2D KH rolls are susceptible to a 3D convective instability (Klaassen and Peltier, 1989; Klaassen and Peltier, 1991), in which the stream-wise vortices stretch and tilt the span-wise vorticity concentrated in KH rolls. Consequently, KH rolls cannot sustain their lateral coherence and break down (e.g., Fritts et al. (1998), Andreassen et al. (1998)). The spanwise instability of KH rolls leads to increasingly complex turbulent interactions and smaller overturning scales, which are likely to modify the amount of mixing with respect to that obtained from 2D simulations (Figs. 2–5 in Özgökmen et al. (2007)). Once the density fronts encounter the

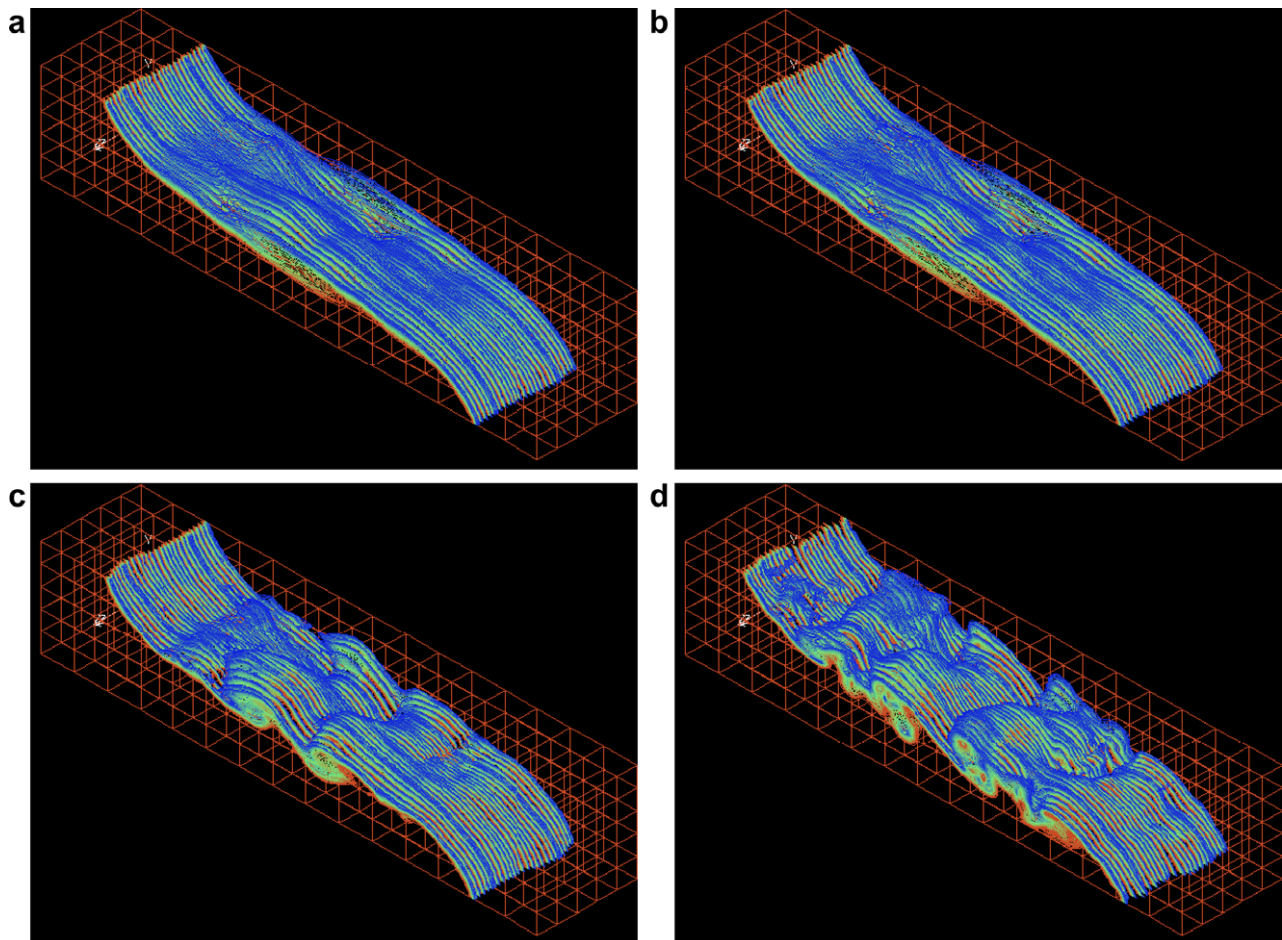


Fig. 6. Density perturbation field $\rho'(x, y, z, t)/\rho_0$ at $t/T_b = 0.61$ from low-res2 LES using (a) SGS-A with $c_s = c_\tau = 0.10$, (b) SGS-B with $c_s = c_\tau = 0.10$ and $Ri_c = 0.25$, (c) SGS-D with $\alpha = 1.2$, and (d) SGS-R with $\gamma = 1$ and $\gamma_\tau = 15$.

lateral vertical walls, they travel almost all the way to the upper domain boundary, and convective instability can be readily observed when the upward motion along the vertical boundaries reverses (Fig. 1c). Towards the end of the simulation, the density perturbation field becomes quite smooth, exhibiting a mixed layer with a thickness of $\approx H/3$ in between the dense and light water masses. Comparison of Fig. 1d to Fig. 2e (or to Fig. 6) in Özgökmen et al. (2007) illustrates that the long-term distribution of ρ' differs in that less mixing is obtained in the 3D than in the 2D lock-exchange problem. Similar results were obtained in Özgökmen et al. (2004a) in terms of reduced entrainment in bottom gravity currents in 3D with respect to that in 2D simulations. This is associated with the onset of the 3D instability in KH rolls.

Snapshots of the density perturbation field from under-resolved simulations are presented in Fig. 2 for low-res1, low-res2 and low-res3 DNS*. They show two main differences with respect to DNS. First, the fields lack high wave number features, and second, the KH rolls appear to be quite coherent laterally. It is not clear a-priori how the long-term mixing will differ with respect to DNS, but we put forth that secondary shear instabilities are not well captured in low-resolution simulations, and therefore they rely more significantly on the span-wise coherent KH rolls to carry out the stirring, which is ultimately leading to the mixing. For resolutions coarser than low-res1, stratified overturns are not captured and the underlying concept of LES fails (as discussed in Section 5.2.4 of Özgökmen et al., 2007). In coarser resolution simulations, either SGS models involving transport equation of turbulent kinetic energy in non-hydrostatic models (so-called very large eddy simulation, VLES,

Ilıcak et al. (2008b)), or conventional turbulence closures in hydrostatic models would be more suitable.

5.1.2. Energetics

It is essential to rely on the energetics of the stratified system in order to arrive at the metrics that help quantify the performance of the different SGS models.

Using the initial density distribution (28) and neglecting the transition layer, which is only 1% of L , the initial total potential energy becomes

$$PE_0 = g \int_V \rho'(x, y, z, 0) z dV = \frac{1}{4} g \Delta \rho' L H^2 W, \quad (33)$$

where V denotes the domain volume. The initial kinetic energy is

$$KE_0 = \frac{1}{2} \int_V |\mathbf{u}(x, y, z, 0)|^2 dV = 0, \quad (34)$$

and the total energy is given by

$$TE = KE + PE. \quad (35)$$

The *background (or reference) potential energy (RPE)* is the minimum potential energy that can be obtained through an adiabatic redistribution of the water masses. In an enclosed and insulated domain with a rigid lid, such as the lock-exchange domain employed here, an increase in the background potential energy can occur only as a result of stratified mixing (Winters et al., 1995). To compute the RPE, we used a probability density function approach introduced by Tseng and Ferziger (2001). In this method,

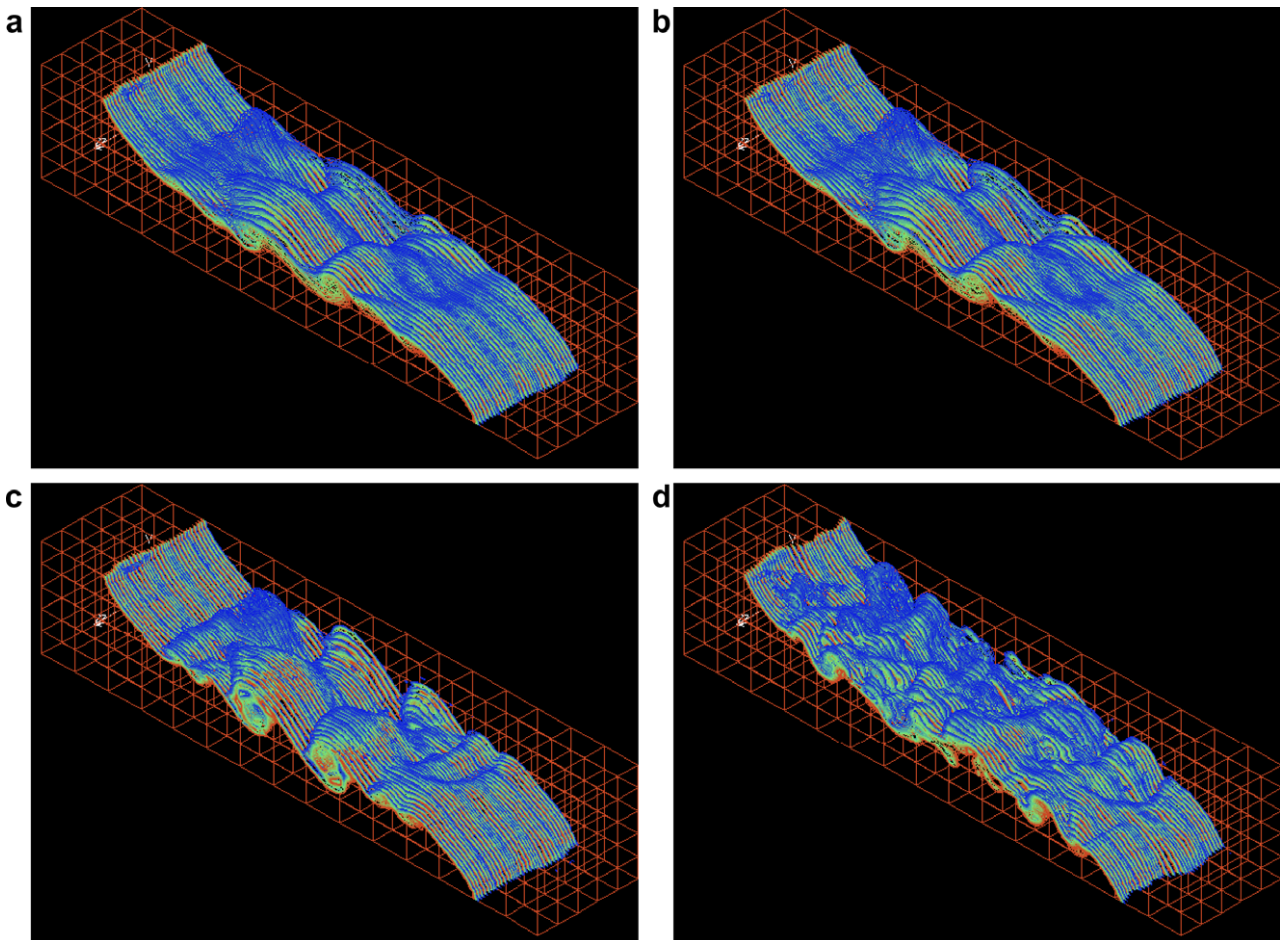


Fig. 7. Density perturbation field $\rho'(x, y, z, t)/\rho_0$ at $t/T_b = 0.61$ from low-res3 LES using (a) SGS-A with $c_s = c_T = 0.10$, (b) SGS-B with $c_s = c_T = 0.10$ and $Ri_c = 0.25$, (c) SGS-D with $\alpha = 1.14$, and (d) SGS-R with $\gamma = 1$ and $\gamma_T = 15$.

the fluid is scanned every time step and the fluid parcels with a density perturbation ρ' within the range of $[0, \Delta\rho]$ are assigned into bins between ρ and $\rho + d\rho$. The normalized number of control volumes in each bin gives the probability density function $P(\rho) = V^{-1} \int_V \delta(\rho - \rho') dV$, where $\delta(\cdot)$ is the Dirac delta function. $P(\rho)$ is the probability of a fluid parcel density to be in the bin of density ρ . Next, we define $z_r(\rho')$ to be the height of fluid of density ρ' in the minimum potential energy state, which can be computed as $z_r(\rho') = H \int_{\rho'}^{\Delta\rho} P(\rho) d\rho$. The background potential energy is calculated from

$$RPE = gLW \int_0^H \rho'(z_r) z_r dz_r. \quad (36)$$

For the initial state, the computation of RPE can be done by inspection, since the density distribution that corresponds to the minimum potential energy is given by

$$\frac{\rho'(z)}{\Delta\rho} \approx \begin{cases} 1 & \text{for } 0 \leq z < \frac{H}{2}, \\ 0 & \text{for } \frac{H}{2} \leq z \leq H. \end{cases} \quad (37)$$

Thus, the initial background potential energy is

$$RPE_0 = \frac{1}{8} g \Delta\rho L H^2 W = \frac{PE_0}{2}. \quad (38)$$

The available potential energy $APE = PE - RPE$ is also equal to $PE_0/2$ initially.

The time evolutions of TE, KE, PE, APE and RPE from high-res DNS are shown in Fig. 3. There are cyclic conversions between KE, PE and APE due to the fluid motion in this enclosed domain, whereas RPE increases monotonically due to irreversible mixing, and TE decreases monotonically due to mixing and dissipation. Therefore, metrics involving RPE and/or TE are better suited to monitor the performance of SGS models than those involving oscillatory behavior due to internal waves and fluid motion.

In order to develop a better understanding of RPE, it is instructive to consider a situation in which mixing has resulted in a constant density gradient zone with thickness 2ℓ in between the dense and light reservoirs,

$$\frac{\rho'(z)}{\Delta\rho} \approx \begin{cases} 1 & \text{for } 0 \leq z < \frac{H}{2} - \ell, \\ 1 - \frac{z - (\frac{H}{2} - \ell)}{2\ell} & \text{for } \frac{H}{2} - \ell \leq z < \frac{H}{2} + \ell, \\ 0 & \text{for } \frac{H}{2} + \ell \leq z \leq H. \end{cases} \quad (39)$$

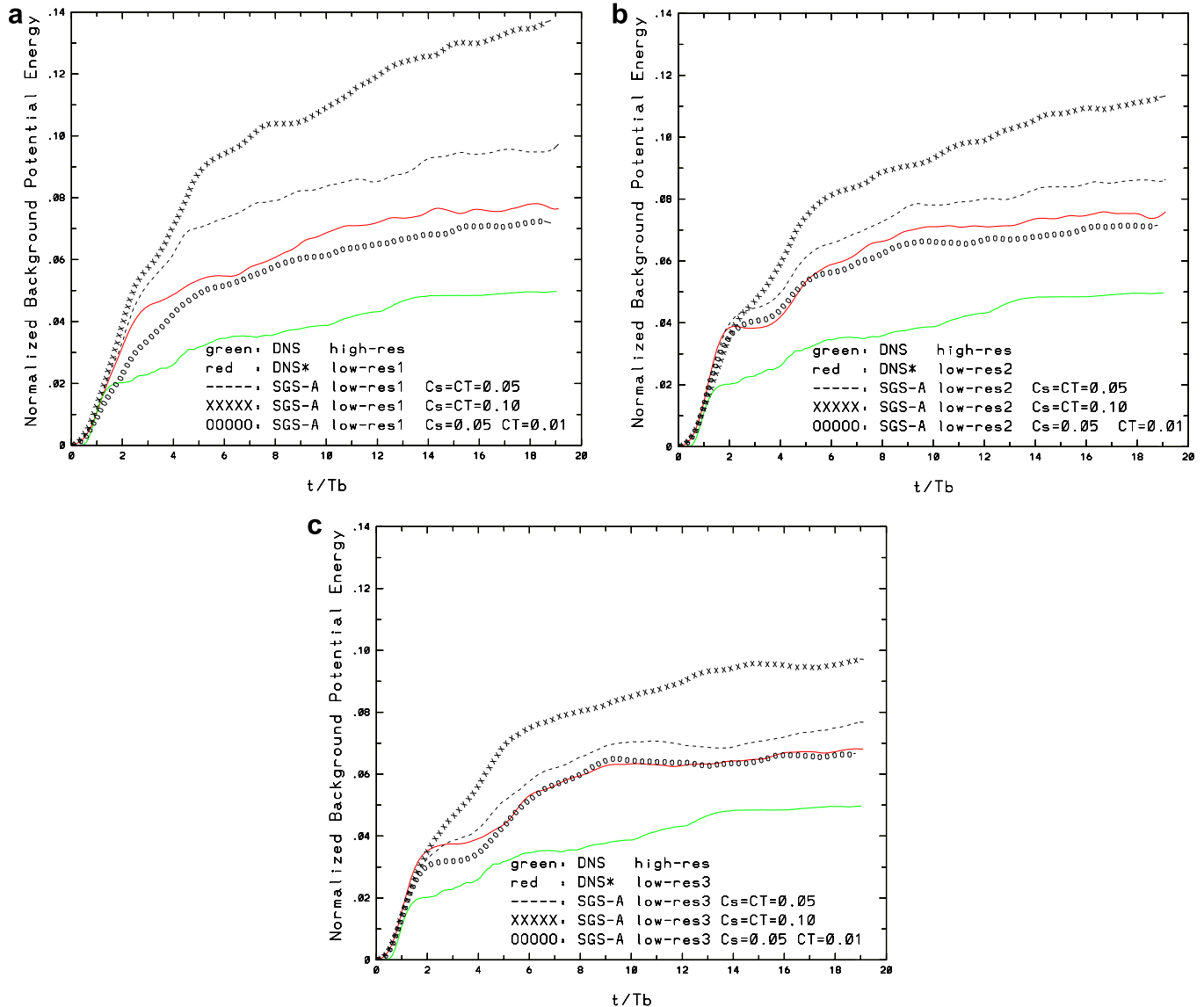


Fig. 8. Time evolutions of the normalized background potential energy RPE* in LES using SGS-A with $c_s = c_T = 0.05$ (dashed lines), $c_s = c_T = 0.10$ (lines with "xxx") and $c_s = 0.05$, $c_T = 0.01$ (lines with "ooo") in comparison to DNS (green line) and experiments without SGS models (red lines) for resolutions (a) low-res1, (b) low-res2, and (c) low-res3. (For interpretation of color mentioned in this figure the reader is referred to the web version of the article.)

In this case, $RPE = g\Delta\rho' LW(\frac{H^2}{8} + \frac{L^2}{6})$. If the entire water column shows a linear density profile, namely $2\ell/H = 1$, then $(RPE - RPE_0)/RPE_0 = 1/3$. Here, an inspection of Fig. 1d indicates only partial mixing with $2\ell/H \approx 1/3$, and therefore we expect $(RPE - RPE_0)/RPE_0 \approx 1/9 \approx 0.1$. We employ the non-dimensional background potential energy

$$RPE^* \equiv \frac{RPE - RPE_0}{RPE_0}, \quad (40)$$

as the primary metric in this study, since it relates directly to irreversible stratified mixing that is of interest in many oceanic problems.

The time evolutions of RPE^* from different resolution DNS* are shown in Fig. 4. Several important points can be observed from this diagram. First, as the spatial resolution is increased, mixing is seen to decrease. This is a somewhat counter-intuitive result, because one would at first anticipate an increase in mixing when more of the turbulent flow features are resolved, which are to engulf more ambient fluid and lead to more mixing. Nevertheless, it turns out that the secondary shear flow instabilities that

are well-captured in high-resolution cases result in a reduced mixing, by disrupting the lateral coherence of the KH billows. Second, the long-term RPE^* settles around $RPE^* \approx 0.075$ for the low-res1 DNS*, while it is $RPE^* \approx 0.05$ for the high-res DNS. Therefore, the difference in mixing between the lowest and highest resolution cases is about 50%, which is quite significant. Third, it is desirable to assess the impact of the high-order polynomial filtering discussed in Section 3 on the solution. This is because this technique can be considered as a form of implicit LES, and it is important to understand how much it influences the solution given that our ultimate objective is to test different SGS models. To this end, we also ran low-res1, low-res2 and low-res3 DNS* with $\beta = 0$, namely without any filtering of the highest order basis polynomial. There seems to be no visible effect on $RPE^*(t)$ (Fig. 4, only low-res1 case is shown) and therefore any changes in mixing can be attributed entirely to the explicit SGS models in the following. Finally, there seems to be only a small difference in $RPE^*(t)$ from med-res2 DNS* and high-res DNS. Thus, the $RPE^*(t)$ from high-res DNS is taken as the benchmark truth, DNS, in the following.

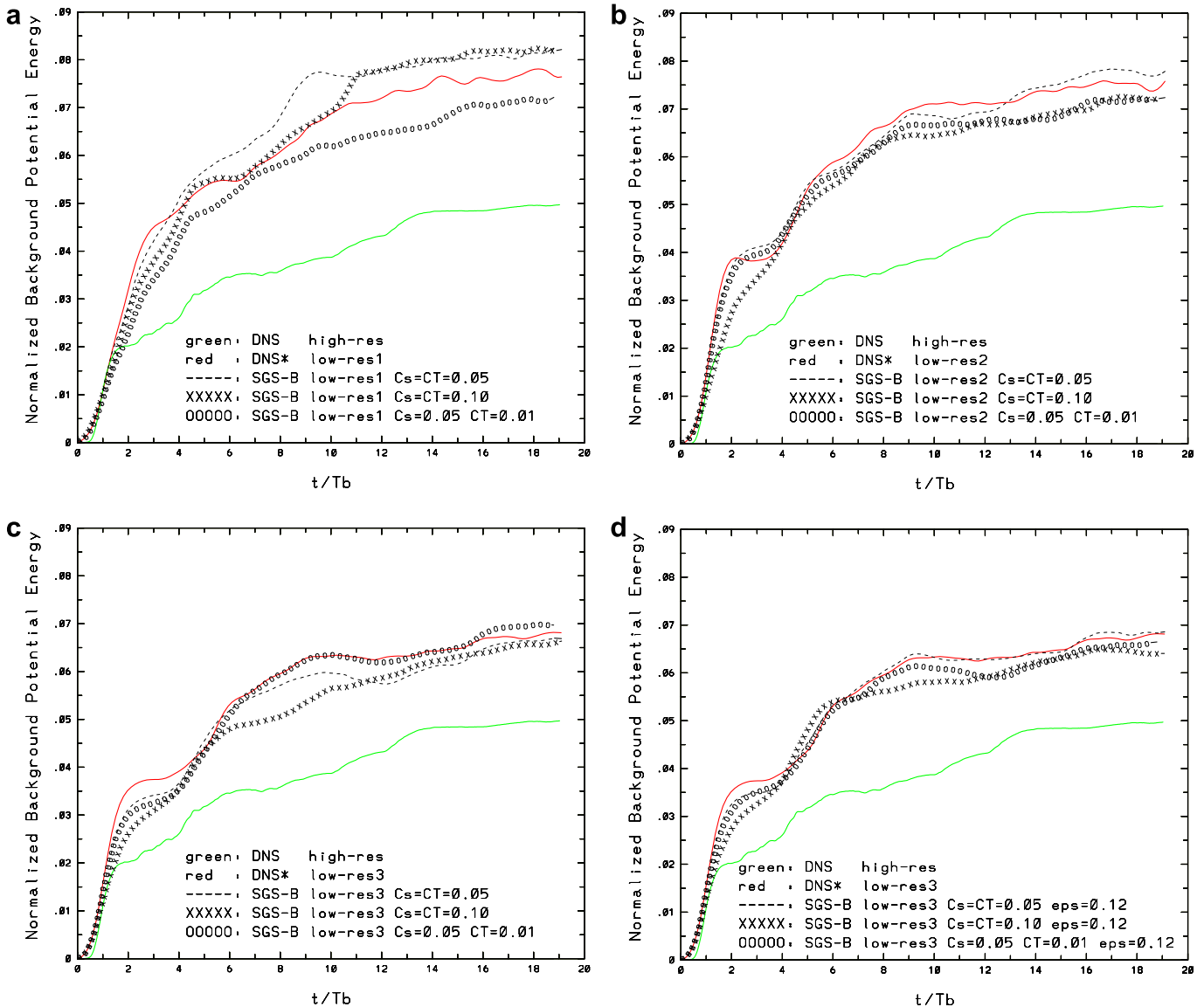


Fig. 9. Time evolutions of the normalized background potential energy RPE^* in LES using SGS-B with $c_s = c_T = 0.05$ (dashed lines), $c_s = c_T = 0.10$ (lines with “xxx”) and $c_s = 0.05, c_T = 0.01$ (lines with “ooo”) in comparison to DNS (green line) and experiments without SGS models (red lines) for resolutions (a) low-res1, (b) low-res2, (c) low-res3, (d) low-res3 but with $\epsilon = 0.12$. In all SGS-B cases, $Ri_c = 0.25$. (For interpretation of color mentioned in this figure the reader is referred to the web version of the article.)

5.2. LES results

5.2.1. Which SGS model performs the best?

The natural first question is which SGS model leads to better results in terms of representing the mixing in this system. This is evaluated in two stages. First, one can qualitatively compare snapshots of the density perturbation fields from LES with different resolutions to DNS* of equivalent-resolution, and also to those from DNS. The LES models are tested on three resolutions, low-res1, low-res2, low-res3 (Table 2), and use the SGS model parameters listed in Table 3. Time snapshots of the density perturbation field ρ' for models SGS-A (4) (with $c_s = c_T = 0.10$), SGS-B (5) (with $c_s = c_T = 0.10$, $Ri_c = 0.25$), SGS-D (12) (with $\alpha = N/(N - 1) = 1.2$ where $N = 6$), and SGS-R (22) (with $\gamma = 1$, $\gamma_T = 15$) are shown in Fig. 5 for low-res1. Several points can be made on the basis of this plot. First, there is no visible difference between SGS-A and SGS-B models at this early stage of the simulation ($t/T_b = 0.61$, Fig. 5a and b). Second, the density interface using SGS-A and SGS-B appears to be smoother than for DNS* (Fig. 2a) at the same

resolution. This seems to be because the growth rate of the instabilities is slower in these LES models, most likely as a result of the excessive viscosity and diffusivity. The density perturbation field from SGS-D (Fig. 5c) has more structure and look closer to the DNS*. On the other hand, the density perturbation field for SGS-R (Fig. 5d) has significantly more structure, not only with respect to all Smagorinsky models, but also DNS*. In fact, the snapshot of the density perturbation from low-res1 SGS-R looks much like the low-res3 DNS* (Fig. 2c). These observations remain valid for all resolutions tested (low-res2 and low-res3 in Figs. 6 and 7, respectively), namely the solutions using SGS-A and SGS-B models appear to be smoother than the DNS* on the same mesh, simulations with SGS-D look visually similar to DNS*, while those using SGS-R resemble higher-resolution DNS*. Clearly, Smagorinsky and rational LES models influence the solution in different ways. Snapshots of ρ' suggest that the former removes the high wave number features of the flow fields while the latter preserves them.

In order to make a quantitative assessment of how the SGS models ultimately influence the stratified mixing, RPE* is plotted

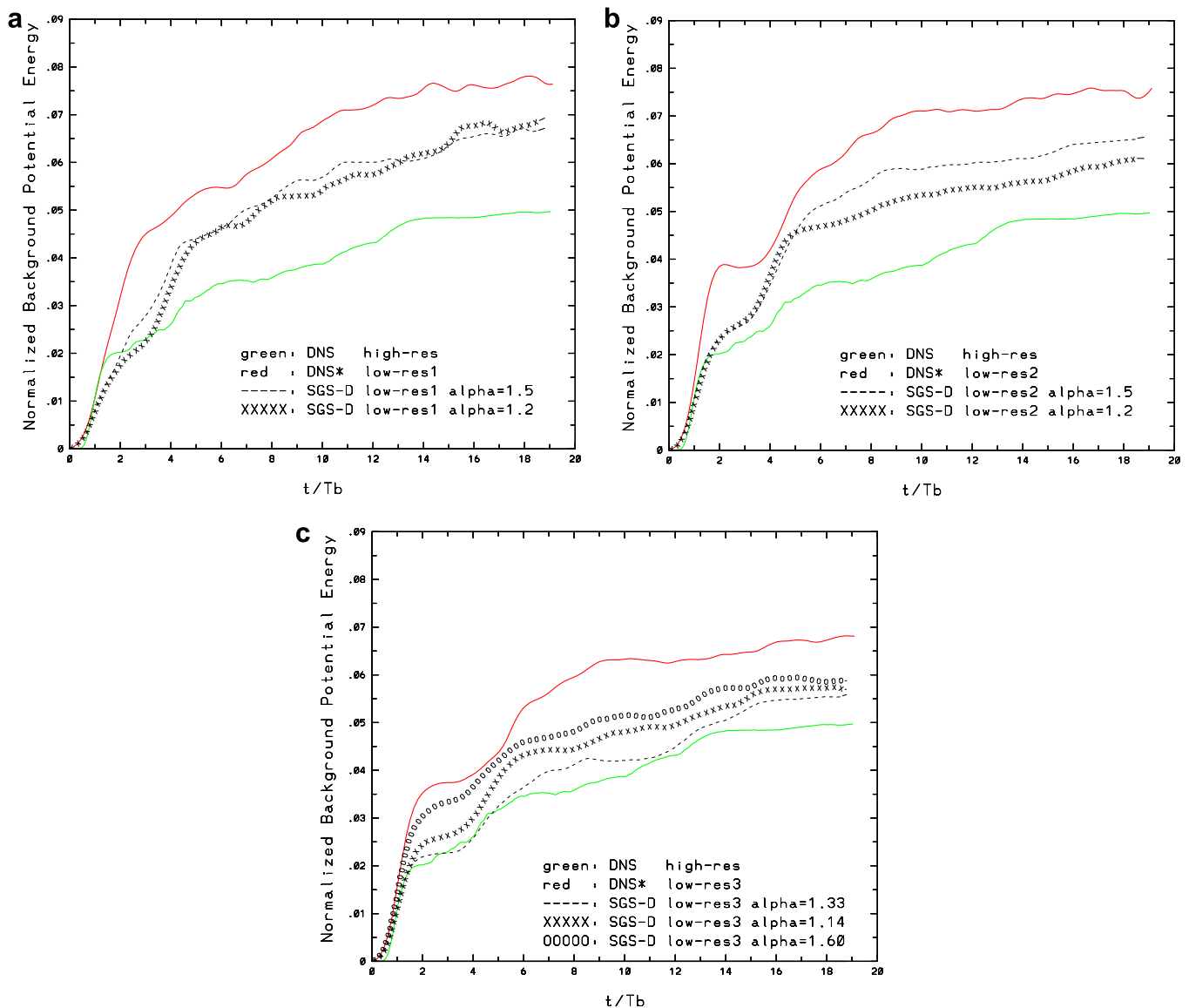


Fig. 10. Time evolutions of the normalized background potential energy RPE^* in LES using SGS-D with $\alpha = N/(N - 1)$ (lines with “xxx”), $\alpha = N/(N - 2)$ (dashed lines), and $\alpha = N/(N - 3)$ (lines with “ooo”), in comparison to DNS (green line) and experiments without SGS models (red lines) for resolutions (a) low-res1, (b) low-res2, and (c) low-res3. (For interpretation of color mentioned in this figure the reader is referred to the web version of the article.)

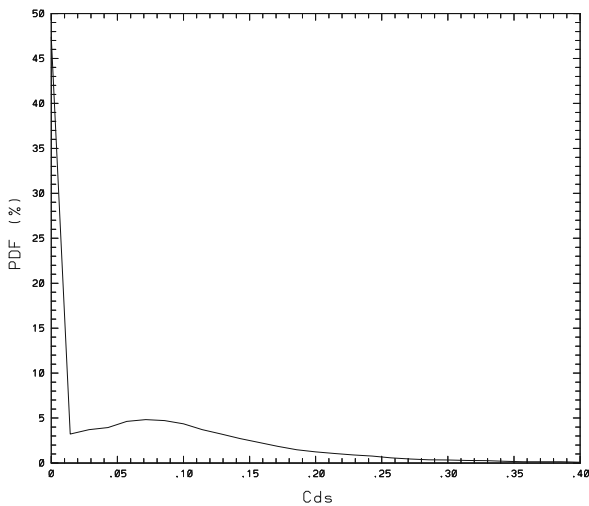


Fig. 11. Time-averaged probability distribution of the dynamic Smagorinsky coefficient C_{ds} from the LES using SGS-D for low-res1.

for each case. Here, an SGS model is considered to improve the solution if it leads to an $RPE^*(t)$ that is in between the envelopes bounded by the DNS and equivalent-resolution DNS* curves. Furthermore, the closer the $RPE^*(t)$ curve is to the DNS curve, the better the SGS model is.

$RPE^*(t)$ from LES using SGS-A with the parameter combinations shown in Table 3 and resolutions low-res1, low-res2, low-res3 are shown in Fig. 8. The cases with $c_s = c_T = 0.10$ and $c_s = c_T = 0.05$ perform worse than the equivalent-resolution DNS*, and the performance gets worse for the higher value of c_s (and c_T). In contrast, the case with $c_s = 0.05$ and $c_T = 0.01$ shows an improvement for low-res1 and low-res2, but not for low-res3.

SGS-B with $c_s = c_T$ leads to slightly worse results than DNS* for low-res1 and to somewhat better results for higher resolutions, low-res2 and low-res3 (Fig. 9a–c). The cases with $c_s = c_T = 0.05$ and $c_s = c_T = 0.01$ are better than both DNS* and those with $c_s = c_T$ at low-res1, but, as in the case of SGS-A, this improvement is not sustained at higher resolutions when SGS-B with $c_s = c_T = 0.10$ leads to the better results. There seems to be little sensitivity of the results to ϵ (the damping parameter in (30)) (Fig. 9d).

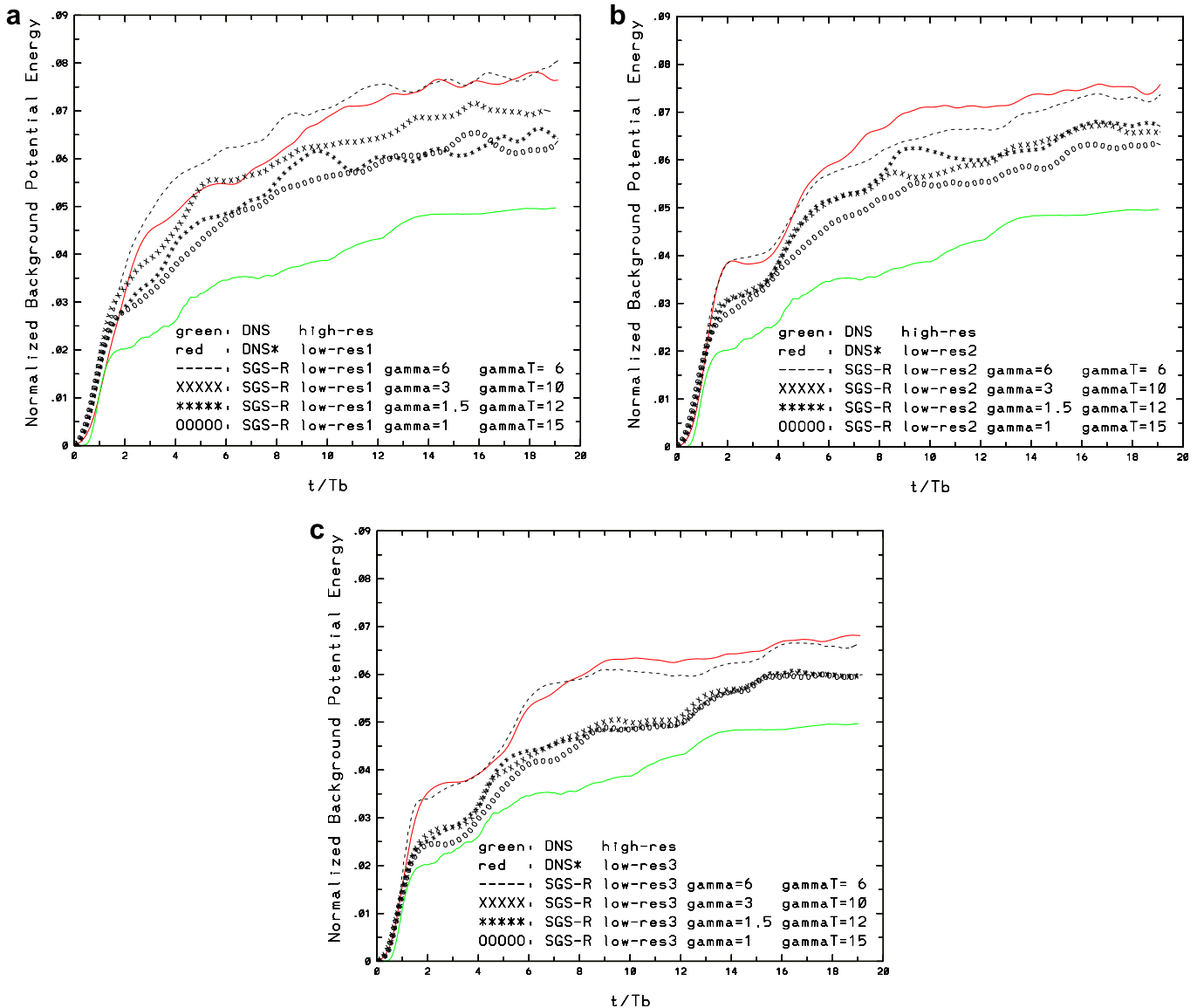


Fig. 12. Time evolutions of the normalized background potential energy RPE^* in LES using SGS-R with $\gamma = 6$, $\gamma_T = 6$ (dashed lines), $\gamma = 3$, $\gamma_T = 10$ (lines with "xxx"), $\gamma = 1.5$, $\gamma_T = 12$ (lines with "*****") and $\gamma = 1$, $\gamma_T = 15$ (lines with "ooo") in comparison to DNS (green line) and experiments without SGS models (red lines) for resolutions (a) low-res1, (b) low-res2, and (c) low-res3. (For interpretation of color mentioned in this figure the reader is referred to the web version of the article.)

The dynamic Smagorinsky model SGS-D clearly results in significant improvements with respect to DNS* (Fig. 10). In fact, it gets quite close to the DNS curve at low-res3 (Fig. 10c). For the coarsest resolution low-res1, there is no significant difference between the two test filters, but for low-res2, the case with $\alpha = 1.2$ performs better with respect to $\alpha = 1.5$, whereas for low-res3, results from $\alpha = 1.33$ are better than those from $\alpha = 1.14$. Since the polynomial order N is different in low-res3 (Table 2), it is not possible to maintain the identical values of α throughout the experiments. But in order to clarify this behavior, an additional experiment is carried out for low-res3 by taking $\alpha = N/(N - 3) = 1.6$. The performance of this experiment is worse than the others. These limited set of experiments suggest $1.2 \leq \alpha \leq 1.33$ as an optimal range of test filter ratios.

An outstanding question is whether the lack of performance in SGS-A is related to our ad-hoc selection of c_s . In order to get a sense of the range of the values calculated for c_{ds} via the dynamic procedure (7)–(10), its probability distribution function (pdf) is plotted (Fig. 11). The pdf is calculated by using a bin size of 0.01, and time averaging, since variability during the evolution of the flow field is found to be quite small. The pdf of c_{ds} has a peak in the range of $0.05 \leq c_{ds} \leq 0.10$, as such in good agreement with the constant values used for SGS-A (Table 3). Nevertheless, the pdf has long tails, reaching values as high as $c_{ds} = 0.40$, and extending in the opposite direction as well. But, the clipping $c_{ds} \geq 0$ used here leads to an accumulation of the pdf at $c_{ds} = 0$. Specifically 47% of all the values for the dynamic Smagorinsky coefficient are set to zero. We interpret this characteristic as an indication of the existence of backward energy cascade in the flow field. Clearly, the dynamic model SGS-D results in a wide range of values so that it is difficult to see how this distribution can be distilled down to a single value for c_s .

Given the novelty of the SGS-R model in the context of stratified flows, it is tested over a wider parameter regime than the other LES models. A sensitivity study with respect to the parameter γ is conducted (Table 3, Fig. 12). Note that, although we assumed the same γ in the momentum and tracer equations when we derived the SGS-R model, in this sensitivity study we considered different values for γ in the two equations. For clarity, we denoted the value of γ in the tracer equation (i.e., in σ_{SGS-R} in (22)) by γ_T . Also note that, by varying γ , in effect we are also varying δ . Indeed, the depen-

dence of the SGS-R model on γ and δ is solely through the factor $\frac{\delta^2}{\gamma}$ in both the Helmholtz operator and the gradient stress tensor (see (22)). Therefore, our sensitivity study with respect to γ is at the same time a sensitivity study with respect to δ . A similar theoretical study was performed by Labovschii and Trenchea (2008) for a different AD model in an entirely different setting. We started with $\gamma = 6$, which is a popular choice (Sagaut, 2006), and $\gamma_T = 6$. It is found that the parameter combination $\gamma = 6$ and $\gamma_T = 6$ does not lead to much difference with respect to DNS*. Then, we gradually reduced γ to 3, 1.5, and finally to 1. We found that SGS-R becomes numerically unstable for $\gamma < 1$. We also found that better results are obtained when $\gamma_T > 6$. Thus, we increased γ_T and decreased γ simultaneously. The best results were obtained for $\gamma = 1$ and $\gamma_T = 15$. The difference of γ and γ_T is likely to be because of the finer features on the density perturbation field than in the velocity field due to $Pr = 7$. As such, a larger value of γ_T leads to a smaller filter factor $\frac{\delta^2}{\gamma_T}$. The RPE*(t) curves converge for smaller values of γ and higher resolutions (Fig. 12c).

The results with the mixed model SGS-M (24) show that while the experiment with $c_T = 0.10$ was not better than DNS* at the same resolution, the case with $c_T = 0.01$ leads to a significant improvement (Fig. 13). Since this result, in addition to the range of γ_T values used above, implies that the SGS stress vectors for the density perturbation may not play an important role in improving LES results, we eliminated these SGS stresses entirely by setting $\sigma = 0$. The results are seen not to change much. Overall, we conclude that the momentum stress tensor τ_{SGS-R} acts to improve the LES solution significantly with respect to DNS*.

Given the wide parameter space covered, we replot the best-performing parameters for each SGS model at each spatial resolution. Fig. 14 shows that SGS-A with different c_s and c_T gives the worst results, and not always better than DNS*. SGS-B represents an improvement over SGS-A, as the results are always better than DNS* and the difference from SGS-A increases with resolution. Both the dynamic model SGS-D and rational model SGS-R lead to significantly better results than DNS*. The best results from the mixed model SGS-M are essentially the same as those from SGS-R (not shown in Fig. 14).

In light of the finding that both the dynamic model SGS-D and rational model SGS-R are effective, yet possess different strengths, namely the former provides adequate dissipation where and when needed, whereas the latter helps preserve the detail of the stratified turbulent coherent structures at coarse resolutions, we put forth the hybrid model SGS-H (25) consisting of the combination of the two as the momentum SGS stress tensor. The stress vector for the density perturbation transport equation is not used, because we were unable to find an effective one on the basis of the above experiments. The main question is whether the combination of SGS-D and SGS-R would give a better result than either one alone. The results shown in Fig. 15 illustrate that this approach indeed works best. In particular, the mixing curve of SGS-H at low-res3 essentially overlaps with that from DNS (Fig. 15c), while running 1212 times faster (Table 4).

5.2.2. Computational overhead of the SGS models

Given that the main objective of LES is to obtain not only better results with respect to DNS*, but also significant computational gain with respect to DNS, it is important to assess the computational overhead of the SGS models. As shown in Table 4, the computations of SGS-A, SGS-B and SGS-D represent only a minor increase of the CPU time, while SGS-H is approximately twice as costly to run as DNS*. Thus, we focused on the computational efficiency of the SGS-R model (22).

An important contribution of this study is the development of a computationally-efficient version of SGS-R. Specifically, we employed a truncated Helmholtz operator as an approximation to the

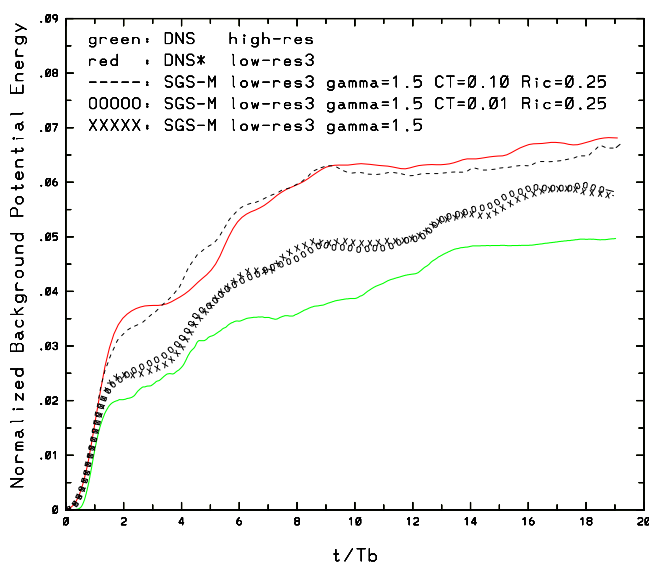


Fig. 13. Time evolutions of the normalized background potential energy RPE* in LES using SGS-M with $\gamma = 1.5$, $c_s = 0.10$ and $Ri_c = 0.25$ (dashed line), $\gamma = 1.5$, $c_s = 0.01$ and $Ri_c = 0.25$ (line with “ooo”), and $\gamma = 1.5$ and $\sigma = 0$ (line with “xxx”) in comparison to DNS (green line) and experiments without SGS models (red lines) for resolution low-res3. (For interpretation of color mentioned in this figure the reader is referred to the web version of the article.)

Helmholtz operator (23) in the SGS-R model. The rationale is straightforward: when using the full Helmholtz operator, the number of iterations needed for convergence is typically 30, which makes the computational time of SGS-R be approximately 8 times higher than that of the corresponding DNS*. This high computational cost was noticed in the previous numerical investigations of SGS-R (Iliescu and Fischer, 2003; Iliescu and Fischer, 2004), but the focus of those studies was on model accuracy rather than efficiency. We also noted that when SGS-R is used with the full Helmholtz operator, the contribution of the SGS stress tensor tends to decrease significantly, yielding results similar to those from DNS*.

Thus, we have experimented with a truncated Helmholtz operator in which only a few iterations were carried out. We found that the optimal choice is with two Helmholtz iterations. By applying just one Helmholtz iteration, the model tends to be numerically unstable, due to the known characteristics of the gradient SGS model. Even with this computational improvement, the cost of SGS-R is high enough to slow down the hybrid model by 1.7–2.0-fold with respect to the equivalent-resolution DNS* for the tested meshes of low-res1 to low-res3 (Table 4). Therefore, the following question arises: *Is it more computationally-efficient to solve the Boussinesq equations using a finer spatial resolution, or to compute SGS-H stresses from a coarser resolution, for a similar RPE*(t) realization?*

To this end, we introduce so-called equivalent-CPU-time DNS*, which have relatively higher resolution but a similar CPU time compared to SGS-H (Table 5). Nek5000 provides dual pathways for convergence, and the CPU time is proportional to KN^4 . As such, one can try to match the CPU time either by increasing the number of elements or the polynomial order. Here, we used the choice that results in the closest CPU time to the SGS-H. As shown in Fig. 16, results obtained by using SGS-H are persistently and significantly better than those from DNS* run on a finer mesh but requires the same CPU time.

6. Summary and conclusions

Modeling of stratified mixing in both coastal and large-scale circulation can benefit greatly from the accuracy of simulations, in which the Boussinesq equations governing the fluid motion are solved subject to as few simplifications and as accurately as possible. However, such high-resolution, non-hydrostatic simulations still represent grand computational challenges for the Re regime

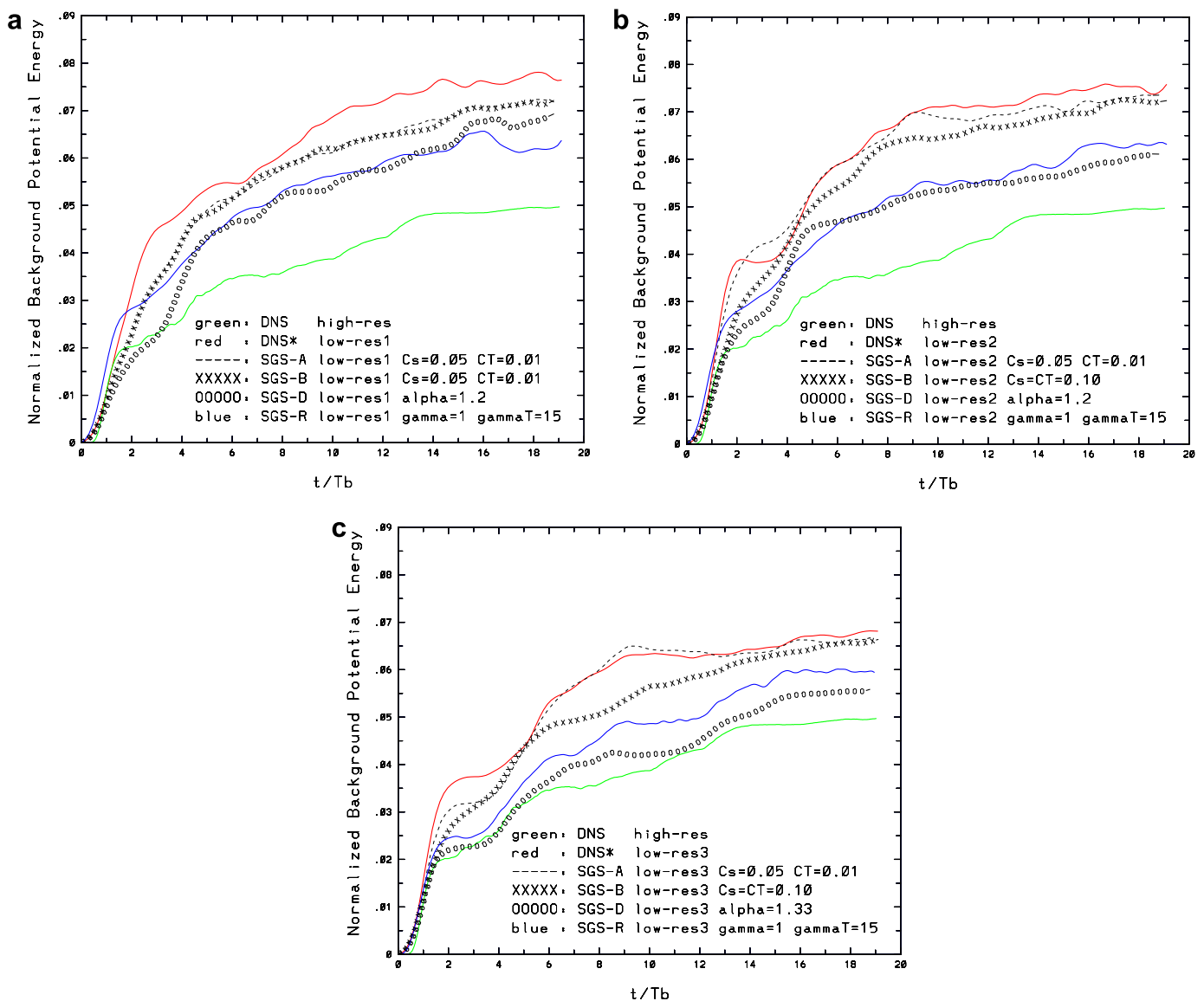


Fig. 14. Time evolutions of the normalized background potential energy RPE^* from SGS models with best performing parameter selections in (a) low-res1, (b) low-res2, and (c) low-res3 LES.

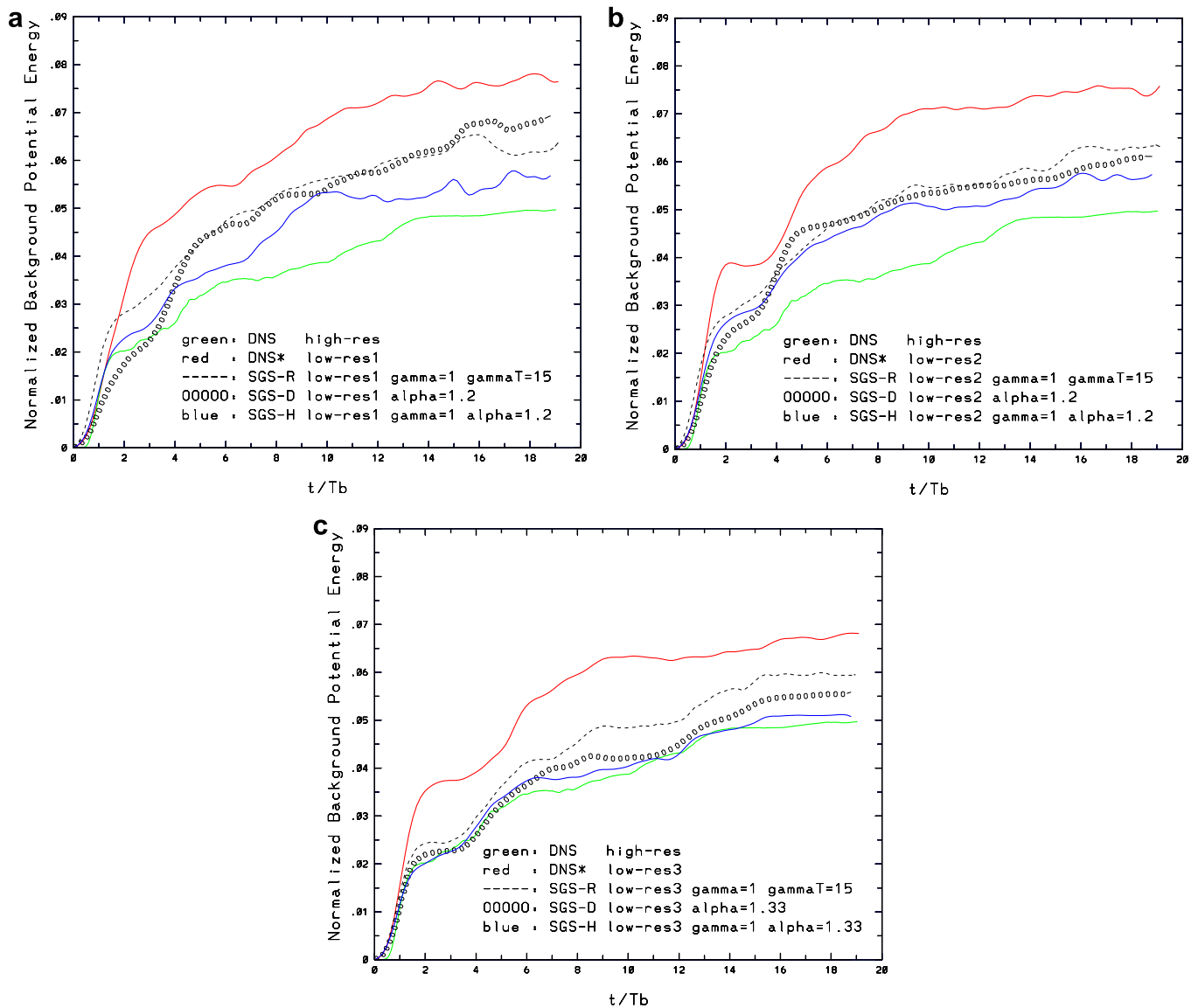


Fig. 15. Time evolutions of the normalized background potential energy RPE^* in LES for resolutions (a) low-res1, (b) low-res2, (c) low-res3, using SGS-H with $\gamma = 1$, $\alpha = N/(N - 1)$ (blue lines) in comparison to SGS-R with $\gamma = 1$, $\gamma_T = 15$ (dashed lines), SGS-D with $\alpha = N/(N - 1)$ (low-res1 and low-res2) and $\alpha = N/(N - 2)$ (low-res3, lines with “ooo”), DNS (green line) and experiments without SGS models (red lines). (For interpretation of color mentioned in this figure the reader is referred to the web version of the article.)

appropriate for oceanic flows. Thus, computationally-efficient approaches need to be developed. LES appears as a natural choice: For homogeneous flows, LES has been highly successful by combining accuracy with computational efficiency. However, only the first few steps have been made in extending the LES methodology to the numerical simulation of stratified flows. It is the goal of this paper to present a thorough *a posteriori* testing of two different classes of

LES models in a benchmark setting to provide future insight for LES of oceanic flows.

As benchmark problem, we use the lock-exchange problem as a canonical test setting for the numerical investigation of mixing in stratified flows. This test problem contains many of the fundamental aspects of stratified mixing, namely vigorous shear-driven mixing, convective motions, internal waves, interactions with

Table 4

The spatial resolutions used for LES. CPU hours needed for each case, computational gain with respect to DNS, and reduction in speed due to the calculation of the SGS stresses are tabulated.

Resolution	SGS model	CPU hours	Computational gain factor wrt DNS	Slow-down factor wrt DNS*
LES low-res1	SGS-A, SGS-B	7.4	12,454	1.2
LES low-res1	SGS-D	7.4	12,454	1.2
LES low-res1	SGS-H	12.4	7432	2.0
LES low-res2	SGS-A, SGS-B	17.7	5207	1.0
LES low-res2	SGS-D	18.9	4876	1.1
LES low-res2	SGS-H	29.1	3167	1.7
LES low-res3	SGS-A, SGS-B	41.6	2214	1.0
LES low-res3	SGS-D	46.0	2003	1.1
LES low-res3	SGS-H	76.0	1212	1.9

Table 5
List of spatial resolutions of DNS* that have approximately the same CPU time as SGS-H. Specifically, the CPU time of low-res4 DNS** compares with low-res1 SGS-H, low-res5 DNS* with low-res2 SGS-H, and low-res6 DNS** with low-res3 SGS-H.

Exp	Resolution	CPU hours	Slow-down factor wrt DNS*
DNS*	low-res4 $K = 192; N = 7; n = 71,485$	13.0	2.1 wrt low-res1 DNS*
DNS*	low-res5 $K = 784; N = 6; n = 179,353$	36.4	2.1 wrt low-res2 DNS*
DNS*	low-res6 $K = 1024; N = 7; n = 367,137$	88.2	2.2 wrt low-res3 DNS*

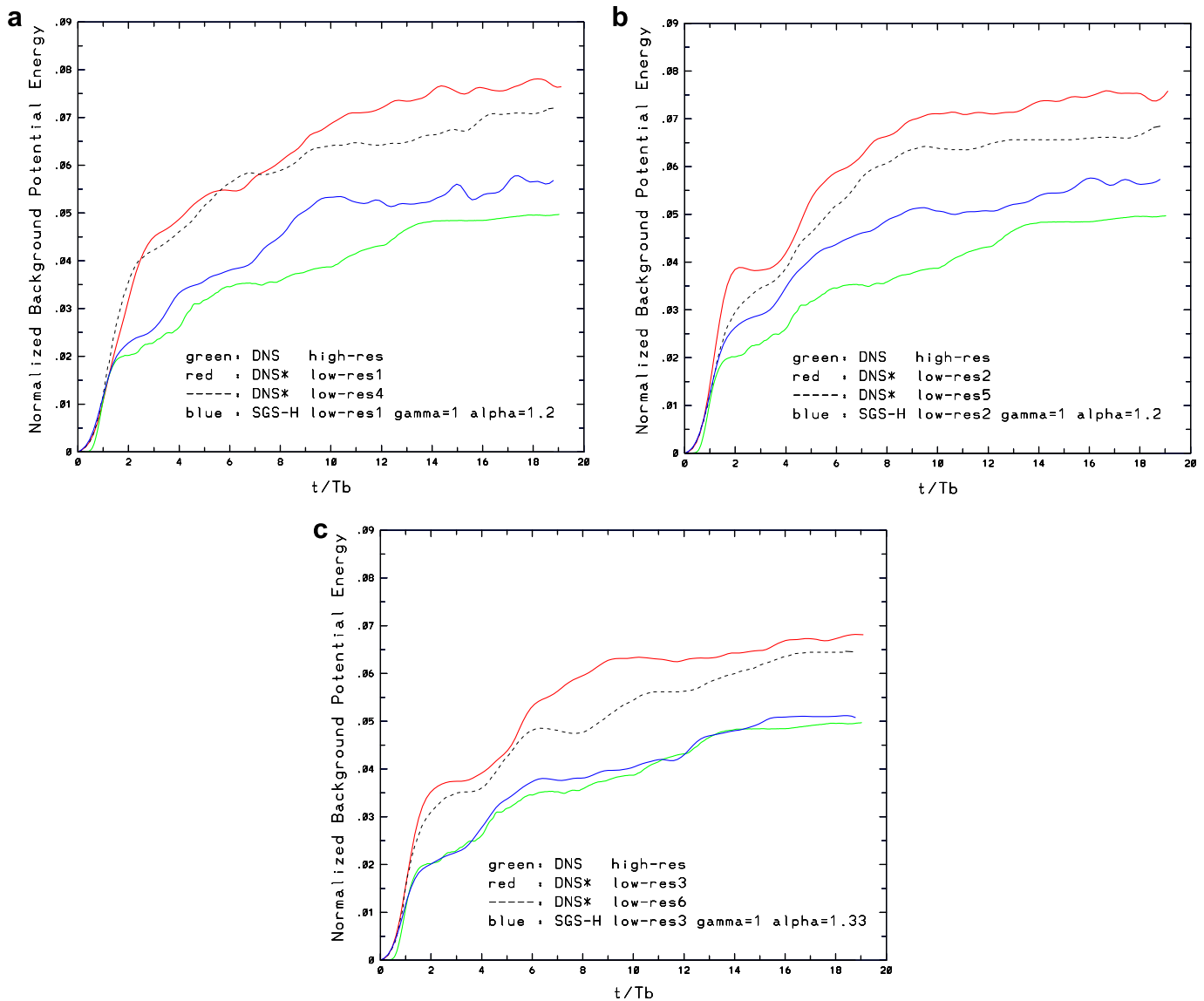


Fig. 16. Time evolutions of the normalized background potential energy RPE^* in LES with best performance, namely SGS-H (blue lines) in comparison to DNS* with equivalent-CPU-time (dashed lines) for resolutions (a) low-res1, (b) low-res2, and (c) low-res3. (For interpretation of color mentioned in this figure the reader is referred to the web version of the article.)

boundaries and transient behavior. At the same time, this setting is extremely simple regarding the domain geometry, initial and boundary conditions, parameters, and forcing. Our main objective is to capture the time-evolution of mixing in this system accurately, while obtaining a significant (on the $\mathcal{O}(1000)$) computational gain with respect to DNS.

To this end, LES are conducted with two different classes of SGS models. The first class consists of Smagorinsky models, the classic

Smagorinsky version SGS-A (4), a modified version Smagorinsky model SGS-B (5), containing an Ri -dependent vertical diffusivity coefficient, and the dynamic version SGS-D (12). The underlying concept of the Smagorinsky model is the existence of an inertial subrange in the energy cascade subject to Kolmogorov's scaling law, and the introduction of eddy-viscosity and diffusivity. The second category consists of SGS-R (22), which is based on the concept of approximate deconvolution of the SGS stress tensor using the

rational approximation of a Gaussian filter (Galdi and Layton, 2000). The SGS stress tensor in SGS-R is of the form of a non-linear gradient model, smoothed by a Helmholtz operator. SGS-R depends neither on the assumption of energy cascade laws, nor on the concept of eddy-viscosity. SGS-R was tested in the numerical simulation of homogeneous turbulent channel flow simulation by Iliescu and Fischer (2003), Iliescu and Fischer (2004), but this is the first time that SGS-R is explored in a stratified mixing problem. A mixed LES model SGS-M (24) employing SGS-R for the velocity SGS stresses and SGS-B for the tracer SGS stresses was tested. Finally, and most importantly, a hybrid model SGS-H (25) is put forward, in which the summation of the dynamic model SGS-D and rational model SGS-R form the subgrid-scale stress tensor for the momentum equations.

These LES models have been implemented in the spectral element code Nek5000 (Fischer, 1997), in which spurious dissipation modes are minimized by the high-order nature of the model. A thorough *a posteriori* testing of the LES models is carried out: LES results are compared to results from both DNS and so-called DNS*, which contain no SGS stresses and are run on three sets of coarse meshes. The main metric of comparison is the background potential energy RPE*, which quantifies the irreversible stratified mixing. Overall, results from 56 3D numerical experiments are compared in this study.

The spatial resolution of DNS* captures the stratified overturning scale, which is the energy containing scale in this problem. Comparison of DNS and different resolution DNS* showed that DNS* overestimate RPE* by approximately 50%. Part of the reason is that secondary instabilities that initiate the 3D cascade of the KH rolls are not well resolved, and the laterally-coherent 2D KH rolls appear to be more effective conduits of stirring and mixing than 3D turbulent features. It is found that SGS-A leads to worse solutions and not always better than DNS*. SGS-B consistently improved the solution with respect to DNS*, but the difference is quite small for the spatial resolutions tested here. In contrast, the dynamical model SGS-D is found to lead to a significant improvement in the prediction of mixing in LES. Similar improvements are also obtained with the rational model SGS-R. It is also found that SGS-R visibly and significantly enhances the high wavenumber features in the density perturbation field with respect to DNS* run at the same spatial resolution. Indeed, the density perturbation fields with SGS-R are very similar to those from higher resolution DNS*. The main conclusion from the experiments with the mixed LES model SGS-M is that we were unable to find an effective SGS model for the density perturbation field in this study. The hybrid model SGS-H produced the most accurate results in predicting the background potential energy RPE*(*t*). In particular, for low-res3 SGS-H yields results of similar accuracy to those from DNS while decreasing the CPU time by a factor of 1212. We also conducted a computational efficiency study and showed that using SGS-H is preferable to running a higher resolution, but equivalent-CPU-time DNS*.

To summarize, the main advance made in this study is the *a posteriori* testing of two fundamentally different classes of SGS models in the LES of stratified mixing in a 3D lock-exchange system. It was found that SGS-A does not provide an improvement with respect to DNS*, SGS-B is marginally better, while SGS-D and SGS-R lead to significant improvements. The two top performers have different strengths: SGS-D provides appropriate dissipation while SGS-R preserves the detail of coherent structures on coarse resolution meshes. As such, it is shown that the superposition of these two models forms an effective and computationally-efficient SGS model. Two significant computational contributions were also made in this study. The first is the high-order adaptation of SGS-D in Nek5000. This makes possible to cover test filter ratios in the range of $1 < \alpha \leq 2$, where we find that values in the lower

half of this range perform significantly better. The second is a numerically-efficient implementation of SGS-R through the use of a truncated Helmholtz operator in (23).

The main outstanding issue is an appropriate SGS model for the density perturbation field σ that would improve the results further. The relatively small effect of σ with respect to τ could be because the regime implied by $Fr = 2^{-1}$ is such that the scales smaller than the size of the stratified overturns are subject to only weak stratification effects (Gargett et al., 1984; Brethouwer et al., 2007). As such, SGS models developed for homogeneous flows appear to be suitable without a significant modification. We plan to investigate how the SGS models tested here would perform in a strongly-stratified flow regime characterized by $Fr \ll 1$ as well. Also, the influence of the viscous-convective subrange that arises in high *Pr* fluids, such as salty water, on mixing, and how this affects development and accuracy of SGS models needs to be studied. Finally, a better near-wall treatment for SGS-R needs to be developed and tested using different boundary conditions and other *Re* regimes.

Acknowledgements

We greatly appreciate the support of National Science Foundation via grants OCE 0620661 and OCE-0620464 under the Collaborative Mathematics and Geoscience (CMG) initiative. We thank Luke Scharf from Virginia Tech's SystemX computational center (www.tcf.vt.edu) for his generous technical help, which made the DNS computation possible. A portion of the computations were carried out on the University of Miami's computing center (<http://ccs.miami.edu/hpc/>), and we thank Nicholas Tsinoremas, Joel Zysman, Ashwanth Srinivasan and Zonghun Hu for their help.

References

- Andreassen, O., Hvidsten, P.O., Fritts, D.C., Arendt, S., 1998. Vorticity dynamics in a breaking internal gravity wave. Part 1. Initial instability evolution. *Fluid Mech.* 367, 27–46.
- Baumert, H., Peters, H., 2004. Turbulence closure, steady state, and collapse into waves. *J. Phys. Oceanogr.* 34, 505–512.
- Baumert, H., Simpson, J., Sündermann, J., 2005. *Marine Turbulence*. Cambridge University Press, Cambridge, UK.
- Benjamin, T.B., 1968. Gravity currents and related phenomena. *J. Fluid Mech.* 31, 209–248.
- Berselli, L., Iliescu, T., Layton, W., 2005. *Mathematics of Large Eddy Simulation of Turbulent Flows*. Springer, Verlag.
- Boegman, L., Imberger, J., Ivey, J.N., Antenucci, J.P., 2003. High frequency internal waves in large stratified lakes. *Limnol. Oceanogr.* 48 (2), 895–919.
- Bourgault, D., Kelly, D.E., 2003. Wave-induced boundary mixing in a partially mixed estuary. *J. Mar. Res.* 51, 553–576.
- Brethouwer, G., Billant, P., Lindborg, E., Chomaz, J., 2007. Scaling analysis and simulation of strongly stratified turbulent flows. *J. Fluid. Mech.* 585, 343–368.
- Britter, R.E., Simpson, J.E., 1978. Experiments on the dynamics of a gravity current head. *J. Fluid Mech.* 88, 223–240.
- Burchard, H., Baumert, H., 1995. On the performance of a mixed-layer model based on the $k - \epsilon$ turbulence closure. *J. Geophys. Res.* 100, 8523–8540.
- Burchard, H., Bolding, K., 2001. Comparative analysis of four second-moment turbulence closure models for the oceanic mixed layer. *J. Phys. Oceanogr.* 31, 1943–1968.
- Cantero, M.I., Balachandar, S., Garcia, M., Ferry, J.R., 2006. Direct numerical simulations of planar and cylindrical density currents. *J. Appl. Mech.* 73, 923–930.
- Cantero, M.I., Lee, J.R., Balachandar, S., Garcia, M., 2007. On the front velocity of gravity currents. *J. Fluid Mech.* 586, 1–39.
- Canuto, V., Cheng, Y., 1997. Determination of Smagorinsky-Lilly constant c_s . *Phys. Fluids* 9 (5), 1368–1378.
- Canuto, V., Cheng, Y., Howard, A., 2007. Non-local ocean mixing mode and a new plume model for deep convection. *Ocean Modell.* 16, 28–46.
- Canuto, V.M., Cheng, Y., Howard, A.M., Esau, I.N., 2008. Stably stratified flows: a model with no $Ri(\text{cr})$. *J. Atmos. Sci.* 65, 2437–2447.
- Canuto, V.M., Howard, A., Cheng, Y., Dubovikov, M.S., 2001. Ocean turbulence. Part I: one-point closure model momentum and heat vertical diffusivities. *J. Phys. Oceanogr.* 31, 1413–1426.
- Cao, C., Holm, D.D., Titi, E.S., 2005. On the Clark- α model of turbulence: Global regularity and long-time dynamics. *J. Turbul.* 6, 1468–5248.
- Carati, D., Winckelmann, G., Jeanmart, H., 2001. On the modeling of the subgrid-scale and filtered-scale stress tensors in large-eddy simulation. *J. Fluid Mech.* 441, 119–138.

- Chang, Y., Xu, X., Özgökmen, T., Chassignet, E., Peters, H., Fischer, P., 2005. Comparison of gravity current mixing parameterizations and calibration using a high-resolution 3d nonhydrostatic spectral element model. *Ocean Modell.* 10, 342–368.
- Clark, R., Ferziger, J., Reynolds, W., 1979. Evaluation of subgrid scale models using an accurately simulated turbulent flow. *J. Fluid Mech.* 91, 1–16.
- D'Asaro, E., Lien, R., 2000. The wave-turbulence transition for stratified flows. *J. Phys. Oceanogr.* 30, 1669–1678.
- Deardorff, J.W., 1974. Three-dimensional numerical study of turbulence in an entraining mixed layer. *Boundary-layer Meteor.* 7, 199–226.
- Deardorff, J.W., 1980. Stratocumulus-capped mixed layers derived from a three-dimensional model. *Boundary-layer Meteor.* 80, 495–527.
- Deville, M., Fischer, P., Mund, E., 2002. High-order methods for incompressible fluid flow, volume 9 of Cambridge Monographs on Applied and Computational Mathematics, Cambridge University Press, Cambridge, ISBN 0-521-45309-7.
- Dörnbrack, A., 1998. Turbulent mixing by breaking gravity waves. *J. Fluid Mech.* 375, 113–141.
- Dryja, M., Widlund, O.B., 1987. An additive variant of the Schwarz alternating method for the case of many subregions. Technical Report Technical Report 339, Dept. Computer Science, Courant Institute.
- Fernando, H.J.S., 2000. Aspects of stratified turbulence. In: Kerr, R.M., Kimura, Y. (Eds.), *Developments in Geophysical Turbulence*. Kluwer, pp. 81–92.
- Ferron, B., Mercier, H., Speer, K., Gargett, A., Poltzin, K., 1998. Mixing in the Romanche fracture zone. *J. Phys. Oceanogr.* 28, 1929–1945.
- Ferziger, J., 2005. Direct and large-eddy simulation of turbulence. In: Baumert, H.Z., Simpson, J.H., Sündermann, J. (Eds.), *Marine Turbulence – Theories, Observations and Models*. Cambridge University Press, pp. 160–181.
- Fischer, P., Gottlieb, D., 1997. On the optimal number of subdomains for hyperbolic problems on parallel computers. *Int. J. Supercomp. Appl. High Perf. Comp.* 11, 65–76.
- Fischer, P., Mullen, J., 2001. Filter-based stabilization of spectral element methods. *C.R. Acad. Sci. Paris Sér. I Math.*, 332 (3), 265–270. ISSN 0764-4442.
- Fischer, P.F., 1997. An overlapping Schwarz method for spectral element solution of the incompressible Navier–Stokes equations. *J. Comp. Phys.* 133, 84–101.
- Fischer, P.F., Miller, N.L., Tufo, H.M., 2000. An overlapping Schwarz method for spectral element simulation of three-dimensional incompressible flows. In: Luskin, P.B.M. (Ed.), *Parallel Solution of Partial Differential Equations*. Springer, Verlag, pp. 159–181.
- Fischer, P.F., Ronquist, E.M., 1994. Spectral element methods for large scale parallel Navier–Stokes calculation. *Computer Methods in Applied Mechanics and Engineering* 116, 69.
- Fringer, O., Gerritsen, M., Street, R., 2006. An unstructured-grid, finite-volume, nonhydrostatic, parallel coastal ocean simulator. *Ocean Modell.* 3–4, 139–173.
- Frisch, U., 1995. *Turbulence, The Legacy of A.N. Kolmogorov*. Cambridge University Press, Cambridge.
- Fritts, D.C., Arendt, S., Andreassen, O., 1998. Vorticity dynamics in a breaking internal gravity wave. Part 2. Vortex interactions and transition to turbulence. *J. Fluid Mech.* 367, 47–65.
- Galdi, G., Layton, W., 2000. Approximation of the larger eddies in fluid motions II. A model for space-filtered flow. *Math. Models Methods Appl. Sci.* 10 (3), 343–350. ISSN 0218-2025.
- Gargett, A., Osborn, T., Nasmyth, P., 1984. Local isotropy and the decay of turbulence in a stratified fluid. *J. Fluid Mech.* 144, 231–280.
- Germano, M., Piomelli, U., Moin, P., Cabot, W., 1991. A dynamic subgrid-scale eddy viscosity model. *Phys. Fluids A* 3, 1760–1765.
- Gibson, C., Nabatov, V., Ozmidov, R., 1993. Measurements of turbulence and fustil turbulence near Ampere seamount. *Dyn. Atmos. Oceans* 19, 175–204.
- Green, M., Rowley, C., Haller, G., 2007. Detection of Lagrangian coherent structures in three-dimensional turbulence. *J. Fluid Mech.* 572, 111–120.
- Hacker, J., Linden, P.F., Dalziel, S.B., 1996. Mixing in lock-release gravity currents. *Dyn. Atmos. Oceans* 24 (1–4), 183–195.
- Hallworth, M.A., Huppert, H.E., Phillips, J.C., Sparks, R.S.J., 1996. Entrainment into two-dimensional and axisymmetric turbulent gravity currents. *J. Fluid Mech.* 308, 289–311.
- Hallworth, M.A., Phillips, J.C., Huppert, H.E., Sparks, R.S.J., 1993. Entrainment in turbulent gravity currents. *Nature* 362, 829–831.
- Härtel, C., Meiburg, E., Necker, F., 2000. Analysis and direct numerical simulation of the flow at a gravity-current head. Part 1. Flow topology and front speed for slip and no-slip boundaries. *J. Fluid Mech.* 418, 189–212.
- Horn, D.A., Imberger, J., Ivey, G.N., 2001. The degeneration of large-scale interfacial gravity waves in lakes. *J. Fluid Mech.* 434, 181–207.
- Hunt, J., Wray, A., Moin, P., 1988. Eddies, stream, and convergence zones in turbulent flows. *Center for Turbulence Rep.*, p. CTR–S88.
- Huppert, H.E., Simpson, J.E., 1980. The slumping of gravity currents. *J. Fluid Mech.* 99, 785–799.
- Ilicak, M., Özgökmen, T.M., Peters, H., Baumert, H.Z., Iskandarani, M., 2008a. Performance of two-equation turbulence closures in three-dimensional simulations of the Red Sea overflow. *Ocean Modell.* 24, 122–139.
- Ilicak, M., Özgökmen, T.M., Peters, H., Baumert, H.Z., Iskandarani, M., 2008b. Very large eddy simulation of the Red Sea overflow. *Ocean Modell.* 20, 183–206.
- Iliescu, T., Fischer, P., 2003. Large Eddy Simulation of turbulent channel flows by the Rational LES model. *Phys. Fluids* 15 (10), 3036–3047.
- Iliescu, T., Fischer, P., 2004. Backscatter in the Rational LES model. *Comput. Fluids* 35 (5–6), 783–790.
- John, V., 2004. Large eddy simulation of turbulent incompressible flows, volume 34 of *Lecture Notes in Computational Science and Engineering*. Springer-Verlag, Berlin, ISBN 3-540-40643-3. Analytical and numerical results for a class of LES models.
- Kantha, L.H., Clayson, C.A., 1994. An improved mixed layer model for geophysical applications. *J. Geophys. Res.* 99, 252355–252366.
- Kantha, L.H., Clayson, C.A., 2000. *Small Scale Processes in Geophysical Flows*. Academic Press, New York.
- Katopodes, F., Street, R., Ferziger, J., 2000. Subfilter-scale scalar transport for large-eddy simulation. In: *14th Symposium on Boundary Layer and Turbulence*. American Meteorological Society, pp. 472–475.
- Klaassen, G.P., Peltier, W.R., 1989. The role of transverse secondary instabilities in the evolution of free shear layers. *J. Fluid Mech.* 202, 367–402.
- Klaassen, G.P., Peltier, W.R., 1991. The influence of stratification on secondary instability in free shear layers. *J. Fluid Mech.* 227, 71–106.
- Kunze, E., Toole, J., 1997. Tidally driven vorticity, diurnal shear, and turbulence atop Fieberling seamount. *J. Phys. Oceanogr.* 27, 2663–2693.
- Labovschii, A., Trenchea, C., 2008. Approximate deconvolution models for magnetohydrodynamics. Technical report, University of Pittsburgh.
- Large, W., Gent, P.R., 1999. Validation of vertical mixing in an equatorial ocean model using large eddy simulations and observations. *J. Phys. Oceanogr.* 29, 449–464.
- Large, W., McWilliams, J.C., Doney, S.C., 1994. Oceanic vertical mixing. A review and a model with a nonlocal boundary layer parameterization. *Rev. Geophys.* 32, 363–403.
- Lavelle, J., Lozovatsky, I., Smith, D., 2004. Tidally induced turbulent mixing at Irving seamount – modeling and measurements. *Geophys. Res. Lett.* 31 (L10308). doi: 10.29/2004GL019706.
- Ledwell, J., Montgomery, E., Polzin, K., St. Laurent, A.R.S.L.C., Toole, J., 2000. Evidence for enhanced mixing over rough topography in the abyssal ocean. *Nature* 403, 179–182.
- Leonard, A., 1974. Energy cascade in large eddy simulations of turbulent fluid flows. *Adv. Geophysics* 18A, 237–248.
- Lesieur, M., 1997. *Turbulence in Fluids*. Fluid Mechanics and its Applications, vol. 40. Kluwer Academic Publishers.
- Lottes, J.W., Fischer, P.F., 2005. Hybrid multigrid/Schwarz algorithms for the spectral element method. *J. Sci. Comput.* 24 (1), 45–78.
- Lueck, R., Mudge, T., 1997. Topographically induced mixing around a shallow seamount. *Science* 276, 1831–1833.
- Maday, Y., Patera, A.T., 1989. Spectral element methods for the Navier–Stokes equations. In: Noor, A.K. (Ed.), *State of the Art Surveys in Computational Mechanics*. ASME, pp. 71–143.
- Maday, Y., Patera, A.T., Ronquist, E.M., 1990. An operator-integration-factor splitting method for time-dependent problems: application to incompressible fluid flow. *J. Sci. Comput.* 10, 496–508.
- Mellor, G.L., Yamada, T., 1982. Development of a turbulence closure model for geophysical fluid problems. *Rev. Geophys.* 30, 851–875.
- Meneveau, C., Lund, T., Cabot, W., 1996. A Lagrangian dynamic subgrid-scale model of turbulence. *J. Fluid Mech.* 319, 353–385.
- Métais, O., 1998. Large-eddy simulations of three-dimensional turbulent flows: geophysical applications. In: Chassignet, E.P., Vernon, J. (Eds.), *Ocean Modeling and Parameterization*, volume 516 of NATO Science Series, Series C: Mathematical and Physical Sciences. Kluwer Academic Publishers, Dordrecht, The Netherlands, pp. 351–372.
- Miles, J.W., 1961. On the stability of heterogeneous shear flows. *J. Fluid Mech.* 10, 496–508.
- Moum, J., Caldwell, D., Nash, J., Gunderson, G., 2002. Observations of boundary mixing over the continental slope. *J. Phys. Oceanogr.* 32, 2113–2130.
- Munk, W., 1966. Abyssal recipes. *Deep-sea Res.* 13, 707–730.
- Munk, W., Wunsch, C., 1998. Abyssal recipes ii: energetics of tidal and wind mixing. *Deep Sea Res.* 45, 1977–2010.
- Nabatov, V., Ozmidov, R., 1988. A study of turbulence over underwater mountains in the atlantic ocean (in Russian). *Oceanology* 28, 210–217.
- Özgökmen, T., Fischer, P., 2008. On the role of bottom roughness in overflows. *Ocean Modell.* 20, 336–361.
- Özgökmen, T., Fischer, P., Johns, W., 2006. Product water mass formation by turbulent density currents from a high-order nonhydrostatic spectral element model. *Ocean Modell.* 12, 237–267.
- Özgökmen, T.M., Iliescu, T., Fischer, P.F., Srinivasan, A., Duan, J., 2007. Large eddy simulation of stratified mixing in two-dimensional dam-break problem in a rectangular enclosed domain. *Ocean Modell.* 16, 106–140.
- Özgökmen, T.M., Fischer, P.F., Duan, J., Iliescu, T., 2004a. Three-dimensional turbulent bottom density currents from a high-order nonhydrostatic spectral element model. *J. Phys. Oceanogr.* 34 (9), 2006–2026.
- Özgökmen, T.M., Fischer, P.F., Duan, J., Iliescu, T., 2004b. Entrainment in bottom gravity currents over complex topography from three-dimensional nonhydrostatic simulations. *Geophys. Res. Letters* 31 (L13212). doi:10.1029/2004GL020186.
- Pacanowski, R.C., Philander, S., 1981. Parameterization of vertical mixing in numerical models of tropical oceans. *J. Phys. Oceanogr.* 11, 1443–1451.
- Patera, A., 1984. A spectral element method for fluid dynamics; laminar flow in a channel expansion. *J. Comp. Phys.* 54, 468–488.
- Peters, H., Gregg, M.C., Toole, J.M., 1989. On the parameterization of equatorial turbulence. *J. Geophys. Res.* 93, 1199–1218.
- Poltzin, K., Toole, J., Ledwell, J., Schmitt, R., 1997. Spatial variability of turbulent mixing in the abyssal ocean. *Science* 276, 93–96.
- Pope, S., *Turbulent Flows*, Cambridge University Press, Cambridge, 2000. ISBN 0-521-59886-9.

- Porté-Agel, F., Meneveau, C., Parlange, M.B., 2000. A scale-dependent dynamic model for large-eddy simulation: application to a neutral atmospheric boundary layer. *J. Fluid Mech.* 415, 261–284, ISSN 0022-1120.
- Raasch, S., Etling, D., 1998. Modeling deep ocean convection: large eddy simulation in comparison with laboratory experiment. *J. Phys. Oceanogr.* 28, 1786–1802.
- Riley, J.J., Lelong, M.-P., 2000. Fluid motions in the presence of strong stable stratification, in: *Annual review of fluid mechanics*, vol. 32, Annu. Rev. Fluid Mech., Annual Reviews, Palo Alto, CA, pp. 613–657.
- Rohr, J.J., Itsweire, E.C., Helland, K.N., Atta, C.W.V., 1988. Growth and decay of turbulence in stably stratified shear flow. *J. Fluid Mech.* 195, 77–111.
- Rottman, J.W., Simpson, J.E., 1983. Gravity currents produced by instantaneous releases of a heavy fluid in a rectangular channel. *J. Fluid Mech.* 135, 95–110.
- Sagaut, P., 2006. Large eddy simulation for incompressible flows. Scientific Computation. Springer-Verlag, Berlin, ISBN 3-540-67890-5. An introduction, With an introduction by Marcel Lesieur, Translated from the 1998 French original by the author.
- Schlatter, P., Stolz, S., Kleiser, L., 2004. LES of transitional flows using the approximate deconvolution model. *Int. J. Heat Fluid Flow* 25, 549–558.
- Schmidt, H., Schumann, U., 1989. Coherent structure of the convective boundary layer derived from large-eddy simulations. *J. Fluid Mech.* 200, 511–562.
- Schumann, U., 1975. Subgrid scale model of finite difference simulations of turbulent flows in plane channels and annuli. *J. Comp. Phys.* 18, 376–404.
- Schumann, U., 1991. Subgrid length-scales for large-eddy simulation of stratified turbulence. *Theor. Comput. Fluid Dyn.* 2, 279–290.
- Shin, J.O., Dalziel, S.B., Linden, P.F., 2004. Gravity currents produced by lock exchange. *J. Fluid Mech.* 521, 1–34.
- Simpson, J.E., 1979. The dynamics of the head of a gravity current advancing over a horizontal surface. *J. Fluid Mech.* 94, 477–495.
- Simpson, J.E., 1987. *Gravity Currents in the Environment and the Laboratory*. John Wiley and Sons, New York.
- Skyllingstad, E., Smyth, W., Moum, J., Wijesekera, H., 1999. Upper-ocean turbulence during a westerly wind burst: a comparison of large-eddy simulation results and microstructure measurements. *J. Phys. Oceanogr.* 20, 5–28.
- Skyllingstad, E., Wijesekera, H., 2004. Large-eddy simulation of flow over two-dimensional obstacles: high drag states and mixing. *J. Phys. Oceanogr.* 34, 94–112.
- Smagorinsky, J., 1963. General circulation experiments with the primitive equations. *Mon. Weather Review* 91, 99–164.
- Stevens, B., Moeng, S.P.P., C.-H. 1999. Large-eddy simulations of radiatively driven convection: sensitivities to the representation of small scales. *J. Atmos. Sci.* 56 (23), 3963–3984.
- Stevens, B., C.-H.M., P. Sullivan. Entrainment and subgrid lengthscales in large-eddy simulations of atmospheric boundary layer flows. In: Kerr, R.M., Kimura, Y. (Eds.), *Developments in Geophysical Turbulence*, Kluwer, 1998, pp. 253–269.
- Stolz, S., Adams, N., 1999. An approximate deconvolution procedure for large-eddy simulation. *Phys. Fluids* 11 (7), 1699–1701.
- Stolz, S., Schlatter, P., Kleiser, L., 2005. High-pass filtered eddy-viscosity models for large-eddy simulations of transitional and turbulent flow. *Phys. Fluids* 17, 065103.
- Thorpe, S., 2005. *The Turbulent Ocean*. Cambridge University Press, New York.
- Thurnherr, A., 2006. Diapycnal mixing associated with an overflow in a deep submarine canyon. *Deep-sea Res. II* 53, 194–206.
- Thurnherr, A., Laurent, L.S., Speer, K., Toole, J., Ledwell, J., 2004. Mixing associated with sills in a canyon on the mid-ocean ridge flank. *J. Physical Oceanogr.* 35, 1370–1381.
- Thurnherr, A., Speer, K., 2003. Boundary mixing and topographic blocking on the mid-Atlantic ridge in the south Atlantic. *J. Phys. Oceanogr.* 33, 848–862.
- Tseng, Y., Ferziger, J., 2001. Mixing and available potential energy in stratified flows. *Phys. Fluids* 13, 1281–1293.
- Tufo, H.M., Fischer, P., 2001. Fast parallel direct solvers for coarse grid problems. *J. Par. Dist. Comput.* 173, 431–471.
- Umlauf, L., Burchard, H., 2005. Second-order turbulence closure models for geophysical boundary layers. A review of recent work. *Cont. Shelf Res.* 25, 795–827.
- Wang, D., McWilliams, J., Large, W., 1996. Large-eddy simulation of the equatorial ocean boundary layer: diurnal cycling, eddy viscosity, and horizontal rotation. *J. Geophys. Res.* 101 (C2), 3649–3662.
- Wang, D., McWilliams, J., Large, W., 1998. Large-eddy simulation of the diurnal cycle of deep equatorial turbulence. *J. Phys. Oceanogr.* 28, 129–148.
- Warner, J.C., Sherwood, C.R., Arango, H.G., Signell, R.P., 2005. Performance of four turbulence closure methods implemented using a generic length scale method. *Ocean Modell.* 8, 81–113.
- Weissel, J.K., Pratson, L.F., Malinverno, A., 1994. The length-scaling properties of topography. *J. Geophys. Res.* 99, 13,997–14,012.
- Wilcox, D., 1998. *Turbulence Modeling for CFD*, second ed. DCW Industries, Inc.
- Winckelmans, G., Wray, A., Vasilyev, O., Jeanmart, H., 2001. Explicit-filtering large-eddy simulations using the tensor-diffusivity model supplemented by a dynamic Smagorinsky term. *Phys. Fluids* 13, 1385–1403.
- Winters, K.B., Lombard, P.N., Riley, J.J., D'Asaro, E.A., 1995. Available potential energy and mixing in density-stratified fluids. *J. Fluid Mech.* 289, 115–128.
- Xu, X., Chang, Y., Peters, H., Özgökmen, T., Chassignet, E., 2006. Parameterization of gravity current entrainment for ocean circulation models using a high-order 3d nonhydrostatic spectral element model. *Ocean Modell.* 14, 19–44.